UNIVERSITA' DEGLI STUDI DI PADOVA

Dipartimento di Ingegneria Industriale

Corso di Laurea Magistrale in

Ingegneria dell' Energia Elettrica

Eccentricity and Stress Analysis in a Reluctance Motor with Finite Element Method

Relatore
Prof. NICOLA BIANCHI

Supervisor
Prof. ANOUAR BELAHCEN

Laureando
GIULIO VARISCO
(2020328)

Anno Accademico 2022/2023

Preface

This thesis is submitted both to University of Padua and Aalto University, school of electrical engineering (ELEC), as the final thesis project for the M.S. course in Electrical Engineering.
I would like to thank both my professor Nicola Bianchi and professor Anouar Belahcen for the trust reposed in me. I'd like to thank my advisor Billah. Thanks to Ahmed, Taha, Nada, Julien, and all the members of the electromechanics building in Maarintie 8. Such a group of talented researchers and people. A challenging place with a great amount of creativeness science should always be acquired of. Not to mention a sincere greeting to my parents who supported me in this journey. Not always this for granted. But hardest way is always the easiest. Now it's better to deal with some more based things, but thanks you all.

Abstract

With the spread of synchronous electrical machines in many industrial applications and vehicle electrification, reluctance motors usage is becoming more relevant. The lack of permanent magnets and their reliability are making them a suitable choice in high speed and torque applications. Besides, because of the rotor configuration made of thin air barriers, noise and vibrations can represent a mechanical drawback. The main source of mechanical vibration is the radial stress due to bearing misalignment and eccentric condition of the shaft. In this thesis the stress at the surface of the stator is computed by means of electromechanics quantities such as radial forces and induction. The computations have been made for different orders of eccentricity. The simulations have been performed with finite element analysis, with FCSMEK software, developed in Aalto University. Therefore the stress frequency domain has been computed in a time-step analysis, with respect to different modes of distribution along the stator surface (modal analysis). Every distribution shows changes in amplitude with the increasing of the eccentricity order. All the quantities have been studied in a Fourier frequency domain to better understand their behaviour and to possibly predict the most significative ones. A clear match between radial forces and stresses is underlined respectively in the frequency domain. Finally the different stresses distribution are analyzed in comparison to the increasing of the eccentricity level.

Sommario

Questo progetto di tesi è stato svolto presso il laboratorio di elettromeccanica di Aalto University, ad Helsinki. Lo studio si propone di analizzare una macchina sincrona a riluttanza a quattro poli e quattro barriere d'aria. Il principale scopo è stato quello di investigare la distribuzione delle forze elettromeccaniche e dello stress da queste derivato alla superficie dello statore, con l'interpretazione delle armoniche più rilevanti per un eventuale continuo del lavoro nella direzione della predizione di guasti. Dato l'attuale sviluppo delle macchine a riluttanza anche in settori commerciali quali gli autoveicoli, dove l'esercizio quotidiano gioca un ruolo importante, disallineamenti negli alberi o eccentricità possono causare vibrazioni e rumore con conseguente messa fuori servizio della macchina. Per questo lo studio dello stress è stato condotto secondo gradi crescenti di eccentricità statica. L'eccentricità statica, ovvero la condizione per cui il centro di rotazione del rotore è spostato radialmente rispetto al centro di simmetria dello statore, rientra nelle condizioni di guasto, di cui ricopre il 60% dei casi. Nello studio predittivo dei guasti generalmente vengono controllate le grandezze meccaniche (le vibrazioni dello statore) o quelle elettriche come le correnti. Nella macchina analizzata lo spettro armonico delle correnti assorbite non ha segnalato cambiamenti significativi tra le condizioni nominali e quelle di guasto. Per questo motivo è stato impiegato un differente approccio che andasse ad indagare direttamente le forze elettromeccaniche coinvolte. Questo anche a fronte della scarsità di risultati presenti in letteratura per questo tipo di macchina. L'analisi dello spettro in frequenza delle forze agenti sulla macchina in condizioni eccentriche, mostra come le armoniche a bassa frequenza (al di sotto di 1kHz) siano le preponderanti. Ciò si nota similmente e coerentemente anche nell'analisi modale dello stress. Ovvero l'analisi di diversi profili di distribuzione spaziale dello stress lungo lo statore. In conclusione i differenti andamenti dello stress meccanico sono comparati in base all'ordine di eccentricità crescente per capire quale modo abbia un andamento preponderante. Dal momento che questi risultati non variano al variare delle condizioni di lavoro della macchina, e vista la relativa bassa frequenza delle principali ar-

moniche di forza, si suggerisce che la natura delle armoniche più rilevanti sia da ricercare nella frequenza di risonanza naturale del sistema rotante.

Contents

Chapter 1

Introduction

1.1 Motivation

With the spread of power electronics in industrial application in the last decades, the usage of synchronous electric motors is becoming frequent. Their possibility to be controlled precisely in term of performance is making them preferable to the induction ones, especially in vehicle and application with high torque and speed demand. In the early 2000's synchronous motor with permanent magnets were the main focus in the market, but the crisis of the rare earth in 2011 made shifting the focus towards synchronous reluctance motors (SynRM), that don't require permanent magnets (they can require cheaper ferrite or less volume magnets in the assisted synchronous reluctance motor). The structure of a SynRM rotor is made of thin canals of air named air-barriers, that create the magnetic poles by a changing in electrical permeability. This configuration can introduce some more fragility from a mechanical point of view so that faulty conditions, like eccentricity, take a relevant place in this kind of machine [1]. This can be a relevant issue if SynRM will take place in the hybridization or electrification in automotive and transportation [2], where daily usage can accentuate bearing misalignment and eccentric conditions of the rotor. Eccentric conditions of the machine's shaft are usually always presence in mechanical rotating parts, even if those are considered acceptable under 10% rate. With daily usage, bearing misalignment and mechanical unbalance can together accentuate this condition. The radial force eccentricity can cause is one of the main cause of mechanical vibration and noise. Usually the main parameters to be controlled in fault diagnosis are current signals from the stator [3] or mechanical vibration [4]. Here a synchronous reluctance machine is analyzed with eccentricity conditions. The machine here under study hasn't shown relevant

changes in current harmonics but only in its fundamental. Since the fundamental is subjected to high variation under load condition, currents were not suitable for fault diagnosis in this case. Vibration was also out of the purpose of this work so that it hasn't been analyzed beforehand. Therefore an electromechanic approach has been chosen instead of the pure electrical or mechanical one. Among the most suitable method for investigating electromagnetic quantities, such as induction and forces, finite element method is utilized. Thus the purpose of this thesis is to study a SynRM with four pole and four air-barriers in different conditions of static eccentricity and therefore the derived stress distribution on the stator surface. Different simulations has been performed in a time-step domain and then the results have been studied in a Fourier frequency domain. The main goal has been to analyze if some patterns in the forces dynamic response and stresses could be possibly useful for a future fault diagnosis. A clear match has been shown between radial forces at 300Hz and 900Hz and the relative stress frequency domain. The tangential force has been neglected since it is more relevant in vibration rather than radial stresses. A similar work has been done in [5] where the dynamic response in terms of forces has been investigated with respect to the eccentricity order. But this has been made only for force itself and permanent magnets machine.

1.2 Structure of the thesis

The thesis has been divided in 7 chapters with the following structure:

- Chapter 1) Motivation and introduction of the thesis.
- Chapter 2) In the first chapter the synchronous reluctance machine is described in its main parameters such as the electromechanics equations and the inner magnetic characterization.
- Chapter 3) In the third chapter the magnetic model described in chapter 2 is extended by introducing the eccentricity condition, following the approach existing in literature.
- Chapter 4) In the fourth chapter some elements of theory are given in order to understand the meaning of the quantities later computed or described. The interaction between magnetic fields and forces is described. The magnetic scalar potential is described as the main unknown in electromagnetics and electromechanics, thus its relationship with magnetic induction.

- Chapter 5) The mechanical stress is introduced and so its interaction with magnetic material. In the second section instead, the stress is presented as result of forces acting on the machine parts. The decomposition of the stress into a space and frequency domain is presented and different modal analysis for the stress distribution are described qualitatively.
- Chapter 6) The machine geometry and parameters are presented. Simulations are presented such as the rated electrical parameters and electromechanic ones like torque ripple, radial forces and stresses distributions.
- Chapter 7) In the last chapter conclusions and further possible development of the thesis are presented.

Chapter 2

Synchronous Reluctance Machine (SynRM)

2.1 Reluctance physic and comparison

In this section 2.1 a brief overview of the reluctance machine would be given. The reluctance machine concept appeared still in the the '900 [6] but has started to be implemented commercially more recently with the Arturo Vagati patent [7]. The main concept relies on the fact that air-filled spaces can introduce an anisotropy in the rotor. Under the magnetization effect of the stator's fields, the flux line are conveyed by those air barriers, so that magnetic poles are induced in the rotor. This lead to absence of permanent magnet usage nor coils winding in the rotor. The main physic concept behind a reluctance machine could be explained by means of energy considerations. In fig. 2.1 three iron object A,B,C are immersed in a magnetic field represented by the dashed lines. Object B is an-isotropic so that its magnetic permeability is grater along d - axe. δ is the angle between d - axe and the main direction of the field n. The concatenated flux between the tree object is maximum when δ tents to zero so that A,B,C are aligned. If the concatenated flux is maximum its derivative is zero. It means that for Faraday law the induced voltage in the core A,C is also zero. Therefore is zero the induced magnetic energy, power and torque between the objects. The concatenated flux is minimum for $\delta = 90°$, and its derivative is at its peak. So that also the torque is maximum when object B is orthogonal to the other ones. The more the anisotropy, the more this effect. The anisotropy introduce a distortion in the magnetic flux line so that the torque tends to reduce this distortion bringing the system to its minimum energy according to the energy conservation law.

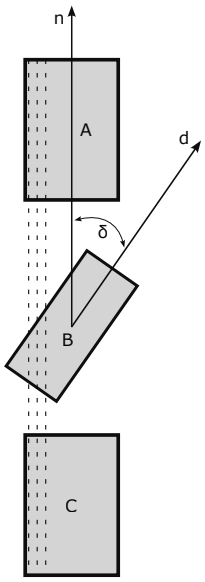

Figure 2.1: Three iron objects immersed in a magnetic field (dashed line). The object in the middle B tents to align to A and C when $\delta \neq 0$. Maximum torque is achieved for $\delta = 90°$.

The model of fig.2.1 is extended to a syncornous reluctance machine. Since the iron magnetic permeability μ is one thousand times greater than air permeability μ_0, the flux lines of B follow the path with higher permeability along the d-axe. This introduces an anisotropy behaviour from the point of view of the magnetic field. Therefore a d-q model is always taken into account to both describe and analyze the machine. The d-axe lay between the two barriers clusters, where the main magnetic flux is spread, fig.2.2

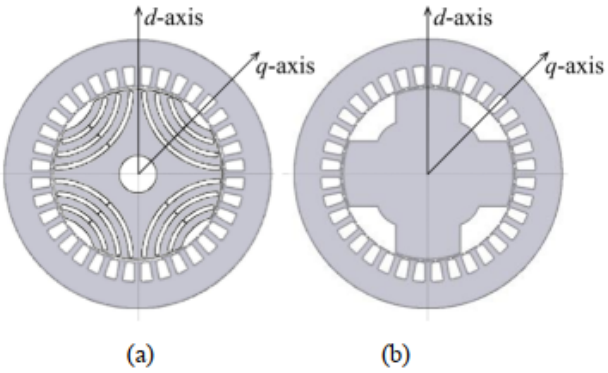

Figure 2.2: Analogy between SynRM (a) and salient-pole (b) configuration [8].

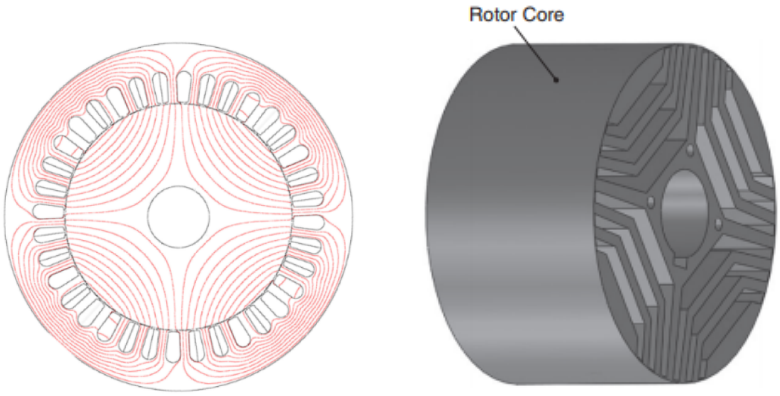

Figure 2.3: Typical magnetic flux behaviour in a 4-pole SynRM [9]. Rotor geometry model on the right.

SynRM are starting to become more used in such applications that require high torque and speed demand. This can represents an advantage since no permanent magnet are used and less rotor losses are involved with respect to induction motor machine. With synchronous machine there is no rotor slip therefore less eddy-current and less losses. SynRM can be 33% smaller in therm of losses [10] with respect to the same power/volt rated IM. For maximizing even more the output in therm of high speed an hybrid configuration between SynRM and permanent magnet synchronous machine (PM) can be taken into account[11]: the permanent magnet assisted SynRM (PMAsynRM). Here the main comparison in terms of efficiency map in fig.2.4.

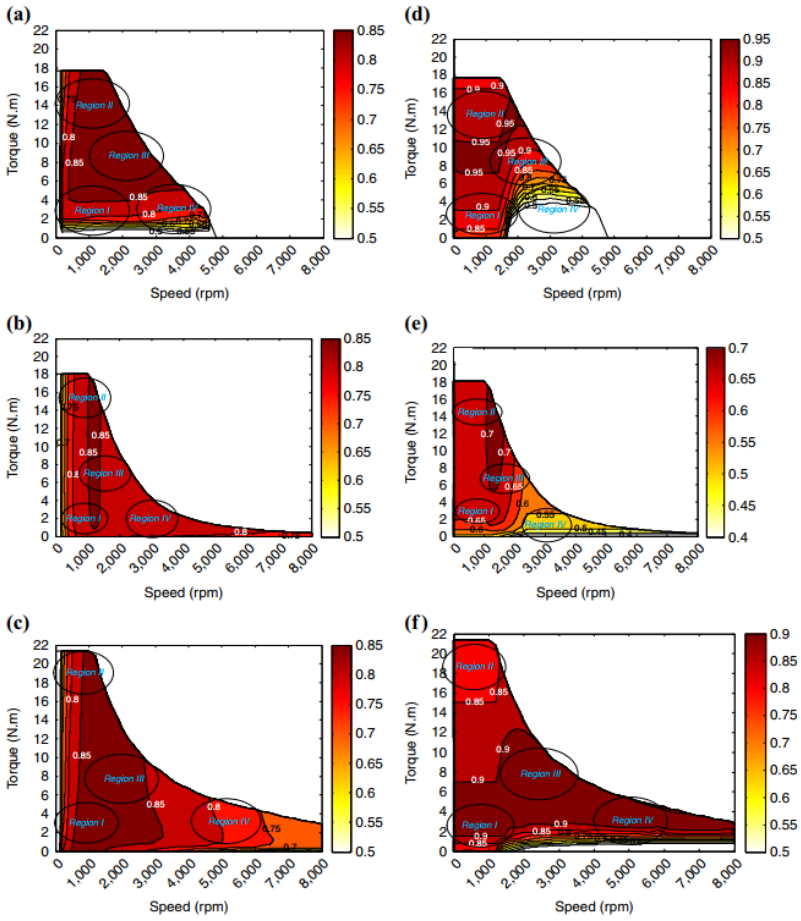

Figure 2.4: First column efficiency map of PM-machine (a), SynRM (b), PMAsynRM (c). Second column, Power Factor map with same machine order [12].

The torque is greater on PMAsynRM because the assisted PM are magnetized in the opposite direction of q-axe so that less saturation lead to more reluctance torque. But still the SynRM torque can be grater than asynchronous induction machine (IM) as stated in [10] by almost 10-20 % for an equivalent rated power IM.
One drawback of the SynRM is the low Power Factor due to the fact that joints between two air barriers saturate, so that more reactive current is required from the armature. See also the difference in angle between current and volt phasor, much larger in the SynRM (fig. 2.5). Thus Power factor can drop to 0.7 for this type of machine. An other drawback is represented by the ribs them self, from a mechanical point of view, but this will be analyzed

more in details in the next chapter.

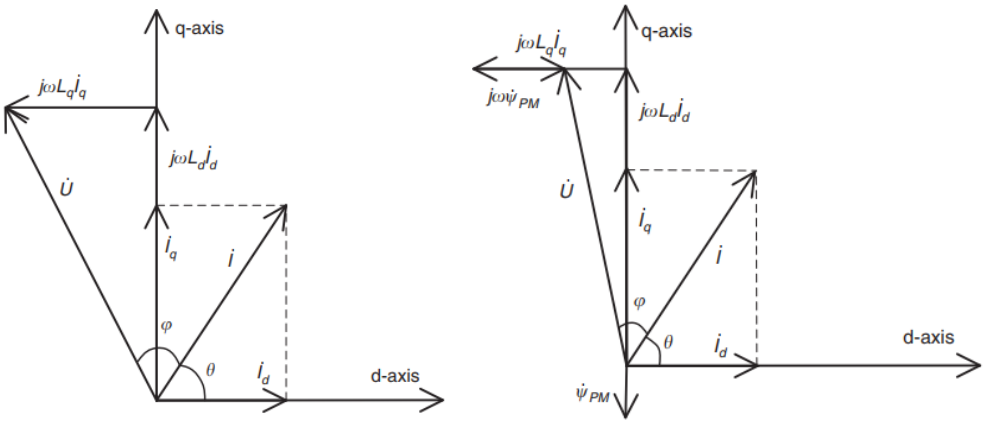

Figure 2.5: Synchronous reluctance on the left and reluctance assisted on the right. On the assisted one the angle between I and U is lower, so the reactive power. Also the q-axe is less saturated since the permanent magnet is magnetized on the opposite of q-axe. This lead to more active current on q-axe, thus more torque with respect to a pure reluctance [12].

2.2 Characteristic SynRM equations

In this section the main SynRM equations will be discussed. Usually this kind of engine are controlled by current source and studied in the d-q model. With both *Clark* ($\alpha - \beta$ system) and *Park* ($d - q$ system) transform, it is possible to reduce a system of 3-phase quantities, time dependent, in two constant variables. So that every spatial vector is made of real and imaginary quantities. In this section the main d-q equations for a SynRM are derived from the most general case.
In the general cases fluxes of a machine can be written as:

$$\begin{cases} \lambda_a = \lambda_m + Li_a \\ \lambda_b = \lambda_m + Li_b \\ \lambda_c = \lambda_m + Li_c \end{cases}$$

With λ_m flux of the d-axe and L mutual inductance. Line voltage in a spatial vector becomes

$$\mathbf{v} = R\mathbf{i} + L\frac{d\mathbf{i}}{dt} + j\omega_m^e \boldsymbol{\lambda} \tag{2.1}$$

with ω_m^e electrical speed. By multiplying this equation for the angle between $\alpha\beta$ and dq frame, $e^{j\theta_m^e}$, it can be written from the stator point of view. Eq 2.1 in its d-q component becomes:

$$v_d + v_q = R(i_d + ji_q) + L(\frac{di_d}{dt} + j\frac{di_q}{dt}) + j\omega_m^e(\lambda_d + \lambda_q)$$

More in particular underlining the cross coupling of the fluxes 2.1 becomes:

$$\begin{cases} v_d = Ri_d + \frac{d\lambda_d}{dt} + j\omega_m^e\lambda_q \\ v_q = Ri_q + \frac{d\lambda_q}{dt} + j\omega_m^e\lambda_d \end{cases}$$

where the the d-q fluxes are given respectively by $\lambda_d = L_d \cdot I_d$ and $\lambda_q = L_q \cdot I_q$

To derive a mechanical behaviour of the machine a power balance can be written as below:

$$\begin{aligned}\frac{3}{2}(v_\alpha i_\alpha + v_\beta i_\beta) = \frac{3}{2}Ri_\alpha^2 + \frac{3}{2}Ri_\beta^2 + \frac{3}{2}L\frac{di_\alpha}{dt}i_\alpha + \frac{3}{2}L\frac{di_\beta}{dt}i_\beta + \dots \\ \dots - \frac{3}{2}\omega_m^e\lambda_{m\beta}i_\alpha + \frac{3}{2}\omega_m^e\lambda_{m\alpha}i_\beta\end{aligned} \tag{2.2}$$

The terms with the resistance are related to the joule losses, the ones with the derivative to the coupled magnetic energies. The last term with the cross dot between fluxes and current is the mechanical power that can be rewritten as:

$$\frac{3}{2}\omega_m^e(\lambda_{ma}i_\beta - \lambda_{m\beta}i_\alpha) = T \cdot \omega_m \tag{2.3}$$

Where T is torque and ω_m mechanical speed. Solving 2.3 for T it can be written as a vectorial product:

$$\begin{aligned}T &= \frac{3}{2} \cdot p(\lambda_{ma}i_\beta - \lambda_{m\beta}i_\alpha) \\ &= \frac{3}{2} \cdot p \cdot Img(\boldsymbol{i} \times \boldsymbol{\lambda_m^*}) \\ &= \frac{3}{2} \cdot p \cdot |\mathbf{i}||\boldsymbol{\lambda_m}|sin(\Delta\theta)\end{aligned} \tag{2.4}$$

where $\Delta\theta$ is the angle between magnetizing flux λ_m and current i. It is at its maximum (maximum torque) when they are orthogonal ($\Delta\theta = \pi/2$). By applying the definition of fluxes in the dq reference, such as $\lambda_d = L_dI_d$ and $\lambda_q = L_qI_q$, 2.4 becomes:

$$T = \frac{3p}{2}(L_dI_dI_q - L_qI_qI_d) = \frac{3p}{2}(L_d - Lq)I_dI_q \tag{2.5}$$

If the total current I is expressed with d-q component, such as $I_d = Icos\alpha_i$ and $I_q = Isin\alpha_i$, torque also becomes:

$$T = \frac{3p}{2}(L_d - Lq)sin2\alpha_i$$

α_i is the angle between the d-axe and the current vector. To derive the maximum torque per ampere behaviour $I_d = Icos\alpha_i$ and $I_q = Isin\alpha_i$ can be introduced in 2.5, therefore deriving with respect to α_i, it can be obtained (also in [13] for permanent magnet motor):

$$\frac{\partial T}{\partial \alpha_i} = 0, \quad cos\alpha_i = \frac{\sqrt{8I^2(L_d - L_q)}}{4(L_d - L_q)} = \frac{\sqrt{2}}{2}$$
$$\alpha_i = 45°$$

This lead to have the maximum torque extracted for each value of current when the current phasor sticks to 45° from the d-axe. A relevant parameter for the saliency ratio. The presence of magnetic poles in the rotor is due to the difference of reluctance of the rotor itself. So that the more is that difference the more is the saliency torque. Other quantities that play a role in the behaviour of the machine are the saliency ratio ξ and the load angle δ here defined as:

$$\xi = \frac{L_d}{L_q}$$
$$\delta = tan^{-1}\left(\frac{\lambda_q}{\lambda_d}\right) = tan^{-1}\left(\frac{1}{\xi}\frac{i_q}{i_d}\right)$$

The load angle is the angle between the main linkage flux $\lambda = \lambda_d + \lambda_q$ and the d - axe. So that δ and α_i can be related by:

$$tan(\delta) = \frac{1}{\xi} tan(\alpha_i)$$

This is used for finding the MTPV condition i.e. the maximum torque extracted for a given voltage. The current angle to impose for this behaviour is also depending on saliency:

$$\alpha_i^{mtpv} = tan^{-1}(\sqrt{\xi})$$

From the power point of view all the angle described play a role into the power factor computation, and so in the overall efficiency.

$$cos\phi = cos(\frac{\pi}{2} - \alpha_i - \delta)$$

The power factor is also dependent on ξ, it has been shown that over ξ = 8-9, the power factor doesn't increase too much anymore. So that usually the saliency ratio doesn't go further 10 or 15, even because it would require too much air-barriers and complexity from a mechanical point of view.

The angles and vectors are summarized in figure below:

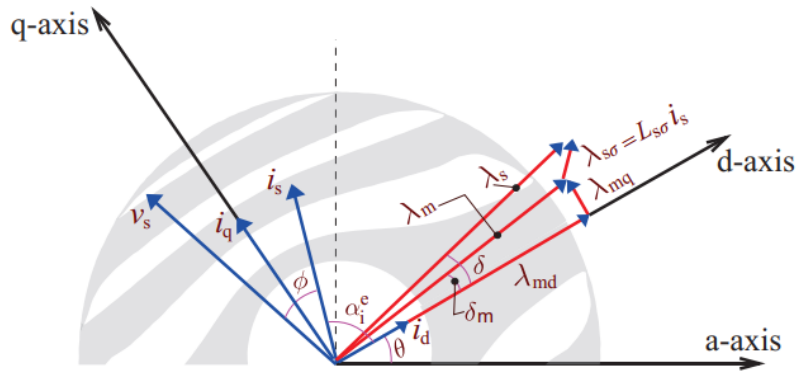

Figure 2.6: Vectorial quantities, here also added the leakage flux $L_{s\sigma}$ [14].

2.3 SynRM Magnetic Equivalent Circuit (MEC)

With the necessity of studying field related quantities all the geometry of the machine has to be taken into account. Integration of quantities over non linear surfaces such as machine's slots is not trivial. Beside, a raw analytical model can be defined with some assumption, such as the linearity of B-H curve and sinusoidal quantities of the magnetic fields.
In such a way it is possible to derive a magnetic equivalent model of the machine. The iron can been seen as a flux generator and the air as a reluctance, thus the the equivalent magnetic circuit can be treated as a circuital one.

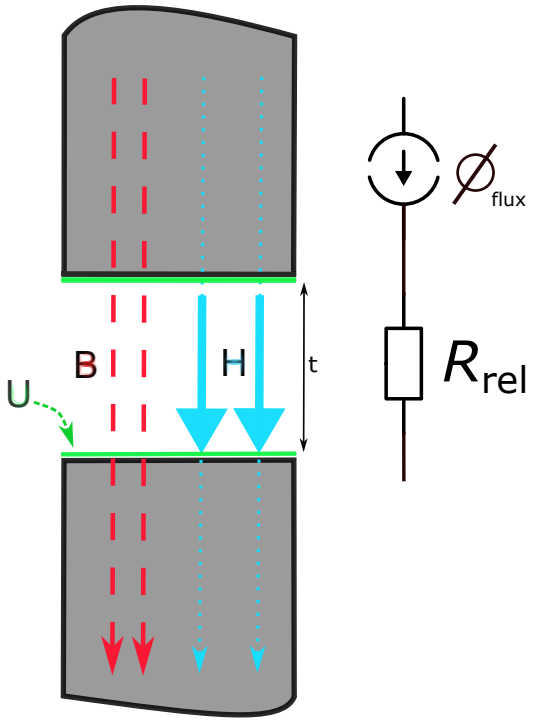

Figure 2.7: Magnetic equivalent circuit scheme.

In fig.2.7 all magnetics quantities such as magnetic field H, magnetic induction B and magnetic scalar potential U are schematized upon an iron core with air-gap t.

With the Gauss and Ampere law the quantities ϕ_{flux} and R_{rel} can be linked to the geometry, and therefore to the machine itself:

$$\Phi_{flux} = \int_{volume} B\, dv$$

$$R_{rel} = \frac{t}{\mu_0 \cdot S}$$

$$\int_{dt} H_{air-gap}\, dt + \int_{dl} H_{iron}\, dl = N \cdot I$$

$$B_{iron} = B_{air-gap} \quad B = \mu H$$

NI will be the total number of conductor times stator current. With the conservation of magnetic induction over the integral path the air-gap induction is derived as $B_t = \mu_0 \cdot NI/t$.
The same model can be applied to a simplified SynRM model where all the quantities are considered sinusoidal for the sake of simplicity.

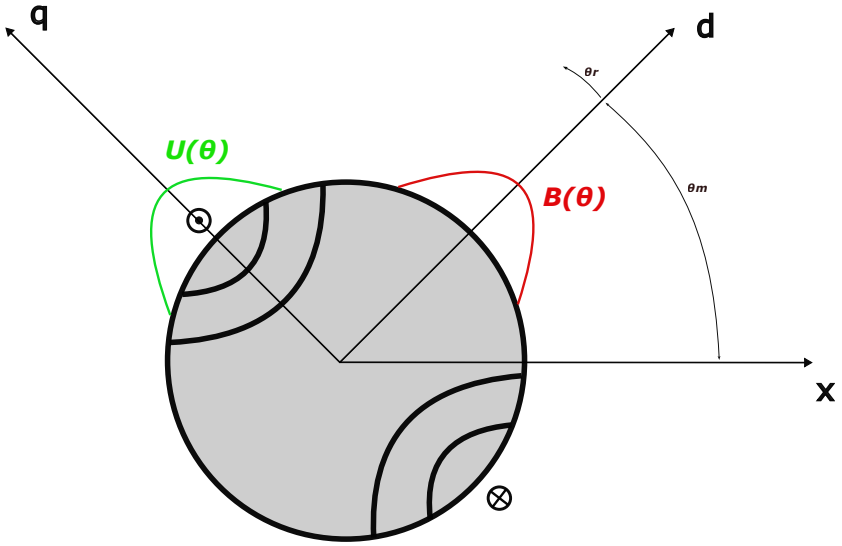

Figure 2.8: Magnetic equivalent circuit scheme applied to the SynRM model. In green the magnetic tension over the rotor barrier. It builds up with the summation of each barrier scalar potential so that a sinusoidal profile can be approximated.

In fig.2.8 the vector scalar potential $U(\theta_s)$ and the induction $B(\theta_s)$ are defined over the rotor in a d-q reference. θ_m is the mechanical angle with respect to a generically x-axe. θ_r is the angle with respect to the d-q frame.

$\theta_s = \theta_m + \theta_r$ is the rotor position seen from a stator reference. Since there are no active source of magnetization in the rotor, the air-gap flux distribution will be related only to the stator winding.

In order to do that the stator current source is defined as proposed in [14]:

$$K_s(\theta_s) = \sum_{\nu^e=1}^{\infty} K_s sin(\nu^e p\theta_s - p\theta_m - \alpha_i)$$

with respect to d-q reference becomes

$$K_s(\theta_r) = \sum_{\nu^e=1}^{\infty} K_s sin(\nu^e p\theta_r + \nu^e p\theta_m - p\theta_m - \alpha_i) =$$

$$= \sum_{\nu^e=1}^{\infty} K_s sin(\nu^e p\theta_r - (\nu^e - 1)p\theta_m - \alpha_i)$$

with p pole pairs, ν^e electrical space harmonic order and K_s current load distribution over the air-gap surface given by:

$$K_s = \frac{3N_s I k_w}{\pi D} \cdot sin\left(\frac{\nu^e \pi}{2}\right) \tag{2.6}$$

$3N_s$ is the total stator conductors, I peak current, k_w winding factor and ν^e number of spacial electrical harmonics. Hence the scalar magnetic potential U[1] can be defined over the position θ_s as an integral quantities:

$$U_s(\theta_s) = \int K_s(\theta_s) \cdot \frac{D}{2}\, d\theta_s$$

with D inner stator diameter.
Since there is no active source of magnetization in the rotor, the air-gap induction B_g is also related only stator's quantities like below, with g air-gap length:

$$B_g(\theta_r) = \frac{-U_s(\theta_r) + U_r(\theta_r)}{g}$$

The quantity U_r can be derived with the pairs of equations below, where the magnetic flux Φ_b is computed from:

[1]Defined as a physical quantities $U_s = H_{stator} \cdot$ Air-gap.

$$\begin{cases} U_r(\theta_r) = \Phi_b \cdot R_b \\ \Phi_b = \int_{\theta_{barrier}} \mu_0 \cdot \frac{-U_s(\theta_r)+U_r(\theta_r)}{g} \cdot \frac{LD}{2}\, d\theta_r \end{cases} \tag{2.7}$$

In fig2.10 a geometry possible way of integration is proposed:

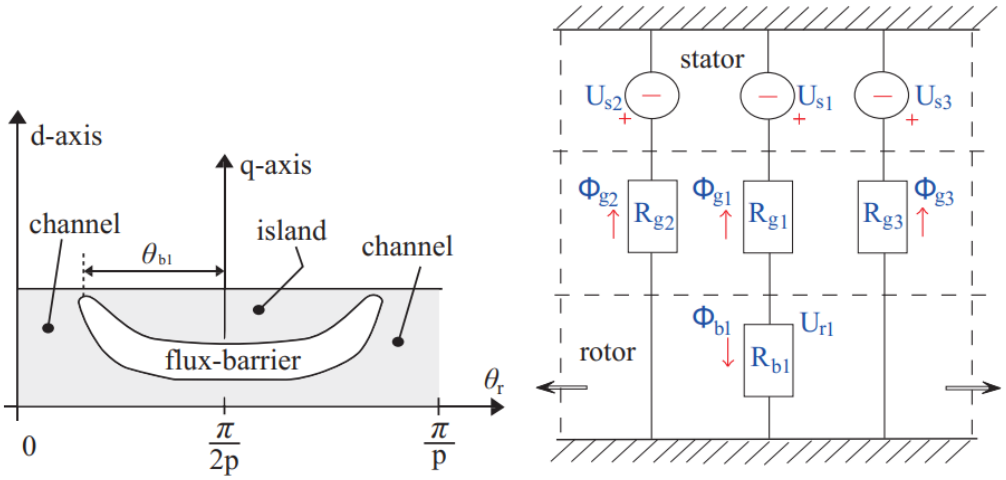

Figure 2.9: Angle of integration on the left and equivalent magnetic circuit on the right proposed in [14].

The key-point in a SynRM MEC is to compute the magnetic scalar potential of the rotor U_r, since this is the only unknown in order to obtain the induction B_g. If it was a machine with a single air-barrier would be simple to solve the MEC of fig.2.10 since each flux generator $\Phi_{g1}, \Phi_{g2}, \Phi_{g3}$ would be decoupled. Because each of those would be attached to the iron armature (ground equipotential).
Hence the Helmholtz magnetic equation could solve each flux as $U_{s1}/(R_{g1} + R_b)$ and son on. Then using these fluxes into 2.7. For a four barriers machine each arm is coupled to each other (see fig.2.10) so that the integration of U_r is mandatory. That's also possible because U_r is considered constant over the position (in the barrier center) so that it can be carried out of the integral as an unknown.

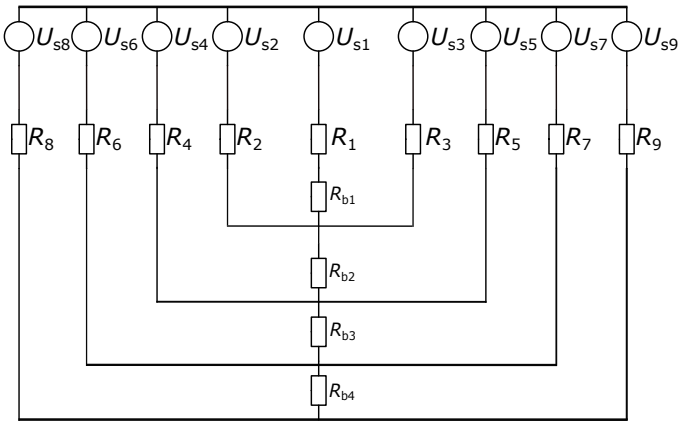

Figure 2.10: Four barriers equivalent MEC.

With the same approach the flux saturation of the iron ribs can be taken into account. A possible approach is proposed in [15]. The ribs induction B_{sat} is supposed near 2 Tesla $(1.8 - 2)$ and its equivalent scalar potential is computed by means of Thévenin equivalent theorem.

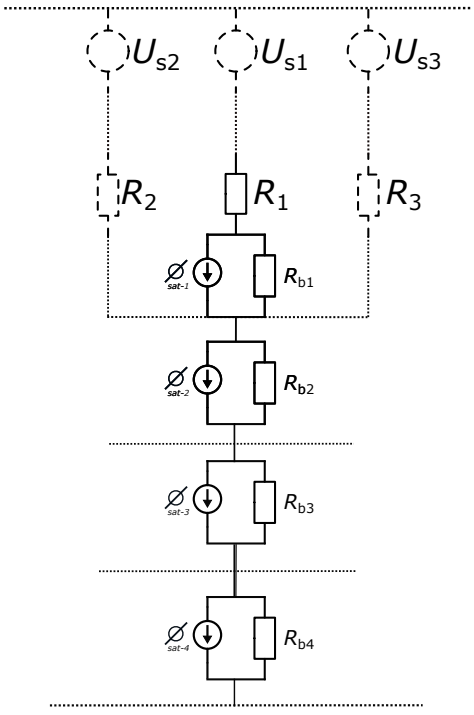

Figure 2.11: Changing in the MEC for taking into account saturation flux that passes through the ribs.

Chapter 3

Eccentricity in SynRM

3.1 Introduction

One of the drawback of SynRM stands from a mechanical point of view. In order to better convey the flux lines, iron ribs between barriers should be as small as possible. Also because if they are small, they can saturate quicker and then absorbing less reactive current. Besides, this can introduce mechanical difficulties since mechanical stress tends to concentrate in the smallest interfaces. Ribs also are a weak point since they are subjected to high tension due to centrifugal forces

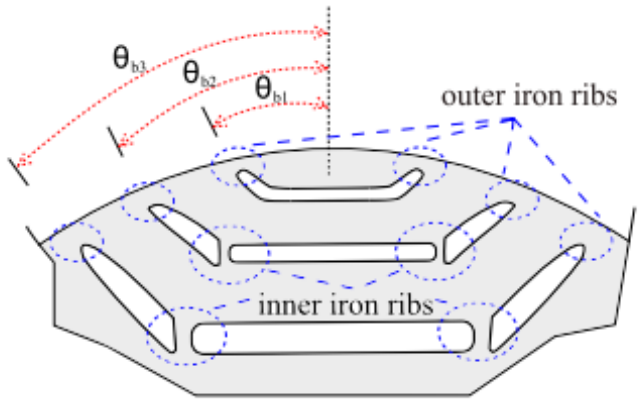

Figure 3.1: On dashed circle the iron ribs where more fluxes in concentrate, more saturation and so also more mechanical stress [16].

The high amount of rotor's saliency could also interact with the stator slot's saliency and yet introducing causes of vibrations. This phenomena can also amplifying the vibration due to mechanical rotor's misalignment. Industrial manufacturing processes could introduce some bearing misalignment [17], also the daily usage of SynRM in electrical vehicle could lead to bearing's unbalance, thus rotor shifting and then eccentricity condition.
The theory of eccentricity has initially been studied from a theoretical point of view since 1918 [18], where the unbalance of the magnetic induction due to eccentricity was studied with geometrical consideration on the B-H curve. The difference from two point in the B-H curve, one in healthy conditions and the other in eccentric ones, was related to the air-gap variation in space. Then the forces related were computed as product between the space and the relative increasing or decreasing of the magnetic fields. More recently eccentricity has been studied analytically in induction motors [19] where the induction in eccentricity condition has been related to the other quantity of the machine like back e.m.f., forces, torque. A relevant amount of studies for induction motors has been validated by Arkkio [20] where forces due to eccentricity at different frequencies were studied and measured. More recently with the spread of finite element simulations the subject has taken a more heuristic approach, also because of the variety of eccentricity, the type of machine and methods of analysis. One of the most common intake is the appearance of magnetic sub-harmonics with order $p \pm 1$, with p pole pairs number, and also the increasing in stresses. This can effects torque ripple and the stress on the machine and so forces, vibration and noise. Thus, for synchronous reluctance and permanent magnet machine, even if the performances like power or torque are subjected to subtle changes, stresses and forces can becomes quite relevant: concerning reluctance machine both static and dynamic eccentricity don't affect the machine performance (besides a slightly increasing of torque ripple). The main aftermath is an increasing of the force towards the smaller air-gap so that "it is imperative to consider the study of eccentricity in these machines because it causes high stress on bearings" [1].

3.2 Eccentricity

Eccentricity can be defined in a general way when the axe of rotation is different from the symmetry axe of the whole system. This condition is common in all mechanical rotating device and can cause up to 60% of faults [21]. Eccentricity can be of three type:

- Static eccentricity (SE): the rotor keeps spinning around its actual axe but it's shifted (and fixed) towards the stator. Caused almost by bearings misalignment.
- Dynamic eccentricity (DE): the rotor's axe rotates around the symmetry axe of the machine, isn't anymore fixed like in the previous case. Caused almost by mechanical unbalance.
- Mixed Eccentricity (ME): it's a combination of both SE and ME: it's a dynamic eccentricity but with the center of rotation shifted radially.

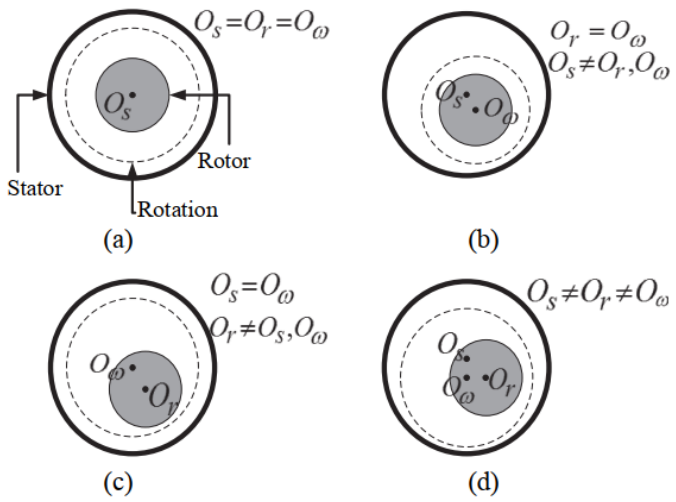

Figure 3.2: Three difference of eccentricity: SE (b), DE (c) and ME (d). Where O_s is the stator centre, O_r the rotor one and O_ω the center of rotation [22].

In this thesis only static eccentricity will be analyzed. A degree of eccentricity is introduced in order do define its variation:

$$\delta = \frac{|g_e - g|}{g} \cdot 100 \tag{3.1}$$

where g_e is the air gap in eccentricity condition and g the air gap in healthy condition. Such as with

$$\delta = \begin{cases} 0 & g_e = g \rightarrow healthy \quad condition \\ 1 & g_e = 0 \rightarrow rotor \quad overlapping \quad stator \end{cases}$$

Eccentricity can also be involved in the axial displacement of the rotor, whether is radial eccentricity or inclined eccentricity. Here only the radial case will be analyzed.

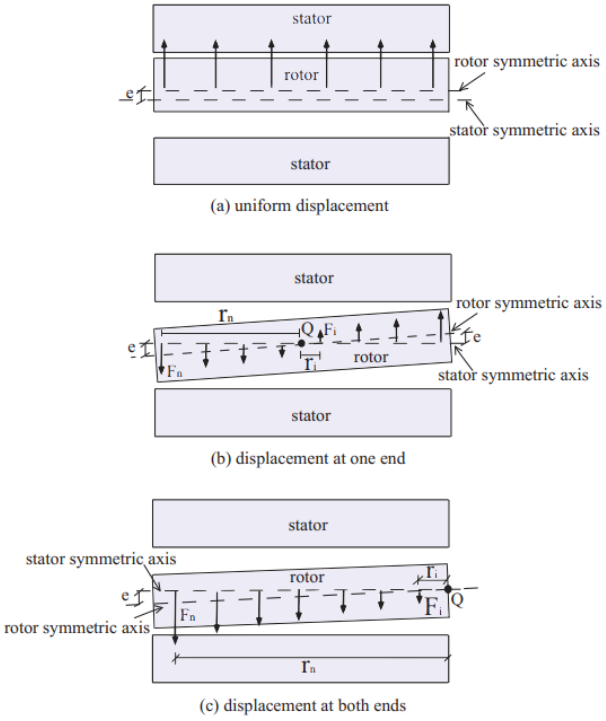

Figure 3.3: a) case of radial eccentricity, b) and c) inclined eccentricity [23].

3.3 Eccentricity Analytical Description

The most evident changing eccentricity can introduce is a variation of the air-gap over the position. In this chapter the analytical model of chapter 2.3 can be extended with static eccentricity as proposed in [23]. Even if in a simplified way for the purpose of this thesis, only for static eccentricity and only acting along x-axe. If the rotor is shifted towards the x-axe, the air-gap reluctance along that direction decrease. Thus more flux density can jump the air-gap and more force is involved. To better describe this phenomena the relative variation δ can be introduced in the air-gap distribution.

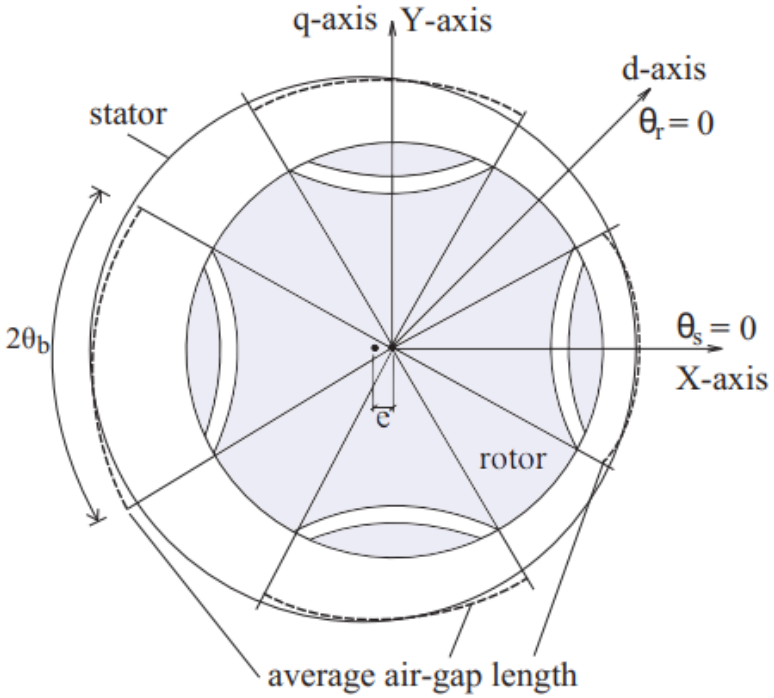

Figure 3.4: Eccentricity model with rotor shifted towards x-axis. Here the eccentricity distance e is equal to $|g_0 - g| = e$. $2\theta_b$ is equal to the angle occupied by the length of a single air barrier [1].

The air-gap g can be expressed as both function of eccentricity order δ and position θ_r as:

$$g(\theta_r) = g(1 - \delta cos(\theta_m + \theta_r)) \tag{3.2}$$

By taking into account the number of air barriers w eq.3.2 becomes:

$$g_w(\theta_m) = g - \left(\frac{\delta}{\theta_b}\right) cos\left(\frac{(2w-1)\pi}{2p} - \theta_e\right) sin\theta_b \tag{3.3}$$

θ_e is the angle between the direction of the eccentricity and x-axe, zero in this case since we assume only radial eccentricity along x. The scalar potential in 2.7 with static eccentricity becomes:

$$U_r^w = -2a_w D \sum_{\nu}^{3} \frac{K_\nu}{(vp)^2} cos(\lambda_{\nu w} \cdot sin(\nu p \theta_b)) \tag{3.4}$$

with coefficients:

$$a_w = \frac{\frac{Dt_b}{2g_w l_b}}{1 + \frac{Dt_b 2\theta_b}{2g_w l_b}}$$

$$\lambda_{vw} = \frac{x(w)\nu^e \pi}{2} + (\nu^e - 1)\omega_m^e t - \alpha_i$$

$w(x)$ is a function that take into account the number of air-barriers, equal to $x = (2w-1)$ with $w = 1, 2, 3...2p$.

K_ν is the fundamental of the load already defined in 2.6. As geometrical parameters of the air-barriers, t_b and l_b are respectively thickness and length as in figure 3.4.

As far as the forces are concerned the Maxwell tensor can be integrated in its radial components and the total force divided into the components F_x and F_y as following:

$$F_x = \frac{DL}{4\mu_0} \int_0^{2\pi} B_g^2(\theta_r) cos\theta_r \, d\theta_r$$

$$F_y = \frac{DL}{4\mu_0} \int_0^{2\pi} B_g^2(\theta_r) sin\theta_r \, d\theta_r$$

As far as the tangential component of the force is concerned it has been shown that it is responsible for 10% of the forces [24]. It is mainly linked to vibration involving half of the value of the magnetic pressure [25].

Chapter 4

A glance to the Finite Element Method

The FEM started to become the most used tool in engineering computation since its ability to solve partial differential equation (PDE) both in space and time. Since the fundamentals of physical quantities (thermal, magnetic, electric, mechanics) can be reduced to the same mathematical expression and still this expression can be approximate just by algebraic equations (polynomial), this method is computationally cheap (and general) to implement. In this chapter the major comcepts and the related magnetic quantities are explained and derived.

4.1 Maxwell Equations

Elctromagnetics forces and quantities are strictly realated to the Maxwell equations and their ability to describe the behaviour of this quantities. Finite elements method is also suitable to solve Maxwell equations in space and time. The literature about it is complete ([26][27][28][29][30]), and that's not the primal goal of this thesis. However the main concepts related to electromagnetics will be presented since they will be utilized by the FEM solver. The basic variables used in Maxwell law are:

E	V/m
H	A/m
D	C/m^2
B	T
J	A/m^2
ρ	C/m^3

Since here we are studying a rotating electrical machine, the Maxwell laws are more suitable in the so called magneto quasi static behaviour. It means that almost all the energy is stored in the magnetic flux line rather than the electric ones. This is the case because an electrical machine is usually compact and more than ten times smaller the electrical wavelength. Furthermore with low frequency (50-60 Hz) capacitance currents are neglected ($\frac{\partial D}{\partial t}$). Taking into account this approximation:

$$\frac{\partial D}{\partial t} \to 0, \quad \frac{\partial B}{\partial t} \neq 0$$

hence, the Maxwell law can be rewritten in their magneto-quasi-static (local) form:

$$\begin{cases} \nabla \times E = -\frac{\partial B}{\partial t} \\ \nabla \times H = J + \frac{\partial D}{\partial t} \\ \nabla \cdot B = 0 \\ \nabla \cdot D = \rho \\ \nabla \cdot J = 0 \end{cases}$$

Since $\nabla \times \mathbf{H}$ is different from zero, is not possible to define the magnetic induction H like a difference of potential. That's reasonable since the majority of FEM codes solve a PDE in the form $\nabla \cdot \nabla F(x, y, z)$ - g = 0. Hence is not possible to reduce the magnetic formulation into a "div-grad" formulation, the most suitable for FEM solver.

4.2 Magnetic vector potential A

The most general expression a FEM solver can solve is something in the form:

$$\nabla \cdot \nu \nabla \mathbf{A} = s$$

where s is the source that produce the field A to solve for. A is dependent on time and space (x, y, z component). This expression is not derivable for the magnetic field at the first insight. That because the rotor of the magnetic induction H is not equal to zero ($\nabla \times \mathbf{H} = \mathbf{J}$ because of Ampere law). Thus magnetic field is not conservative and can't be expressed as a difference of potential, nor as a gradient of something. To overcome this, the mathematical operator A is introduce so that $\mathbf{A} = \nabla \times \mathbf{B}$. The magnetic vector potential A is defined as:

- Defined in space as $A(x, y, z)$.
- Not unique, so that many $\mathbf{A}$ are possible.
- Defined as $\mathbf{A} + \nabla\Phi$, where Φ is an arbitrary scalar function.

To manage the non uniqueness of the vector potential, the one with zero divergence is chosen ($\nabla \cdot \mathbf{A} = 0$). With the previous definitions and tanking into account the material law $\mathbf{H} = \nu\mathbf{B}$, the Ampere law becomes:

$$\rightarrow \nabla \times (\nabla \times \mathbf{A}) = \mu J \tag{4.1}$$

With μ magnetic permeability. Since in electrical machine the flux is usually radial and constant along their length (z-axe), the 2D case is almost always assumed. In 2D the induction becomes:

$$\mathbf{B} = \mathbf{B}(B_x, B_y, 0) \tag{4.2}$$

$$\mathbf{A} = A(0, 0, A_z) \tag{4.3}$$

Because the induction lays on a x-y plane, and since B is also the curl of A, the potential A has only one component along z. This actually simplifies the computation. By actually computing B becomes:

$$\nabla \times \mathbf{A} = det \begin{bmatrix} i & j & k \\ \frac{\partial}{\partial x} & \frac{\partial}{\partial y} & \frac{\partial}{\partial z} \\ 0 & 0 & A_z \end{bmatrix} = \dots$$

$$\cdots = \left(\frac{\partial A_z}{\partial y}, -\frac{\partial A_z}{\partial x}, 0 \right) = (B_x, B_y, 0) \tag{4.4}$$

Since A has only the z component, it's easy to compute its gradient as:

$$\nabla A_z = \left(\frac{\partial A_z}{\partial x}, \frac{\partial A_z}{\partial y} \right) \tag{4.5}$$

Equations 4.4 and 4.5 are the same only with switched order of x and y. It means that in 2D the induction B is actually the gradient of A just switched of 90° degree as shown in figure.

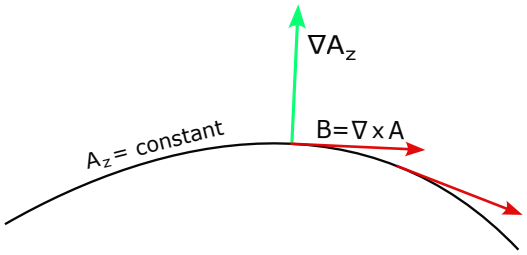

Figure 4.1: Black line equipotential of A_z, green line the gradient of A_z and the red one shows the gradient rotated of 90°, i.e. $\nabla \times \mathbf{A}$.

To derive the final form of the PDE suitable for the fem solver, the 4.4 with the Ampere law becomes:

$$\begin{aligned} \mathbf{H} &= \nu \left(\frac{\partial A_z}{\partial y}, -\frac{\partial A_z}{\partial x}, 0 \right) \\ \nabla \times \mathbf{H} &= det \begin{bmatrix} i & j & k \\ \frac{\partial}{\partial x} & \frac{\partial}{\partial y} & \frac{\partial}{\partial z} \\ \nu \frac{\partial A_z}{\partial y} & -\nu \frac{\partial A_z}{\partial x} & 0 \end{bmatrix} = \\ &= k \left(-\frac{\partial (\frac{\nu \partial A_z}{\partial x})}{\partial x} - \frac{\partial (\frac{\nu \partial A_z}{\partial y})}{\partial y} \right) = J_z \end{aligned} \tag{4.6}$$

Equation 4.6 is also a summation of derivatives of the function ∇A_z, so that it can be seen as a divergence of ∇A_z. Eq. 4.6 is also equal to the z-component of the current J so that 4.1 can be reduced to its equivalent "div-grad" form:

$$\nabla \cdot (\nu \nabla A_z) = -J_z \tag{4.7}$$

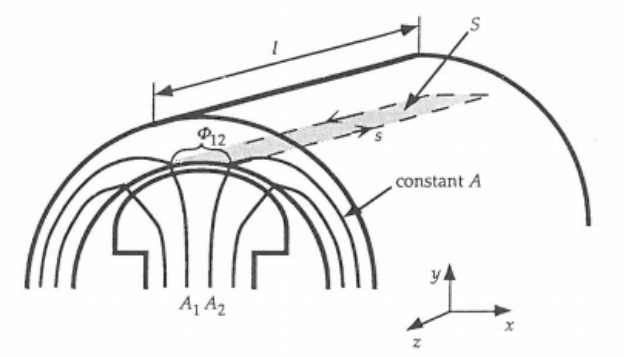

Figure 4.2: Line of A_z in a electrical machine [28].

Where ν is the magnetic susceptibility and J_z the current source. A_z is then solved for each point of the domain. In order to define a unique solution the behaviour of the field in the domain boundaries has to be defined. Usually in electrical machine the "magnetic insulation" or Dirichlet condition is imposed as $A_z = 0$ in the interfaces with air as along the external boundaries of the stator. It stated that all the line are conveyed within the iron and there is no field leaking out of the stator like in fig. 4.2.

4.3 FEM formulation

The mathematical formulation for the finite element method is quite complex. Here a glance is given on how is possible to switch from the "dive-grad" form to an algebraic linear system, more suitable for the numerical solver. The value of a field U for each point of a 2D domain Ω is given by the function $U(x, y) \quad \forall x, y \in \Omega$.
The domain is discretized with a number of elements e and node i, and for each element a shape function is defined. In 1D the shape function $N_i(x)$ is equal to one in the node i and zero on every other node. It is build by straight line if the elements are of the first order or by quadratic curves if the order is greater.

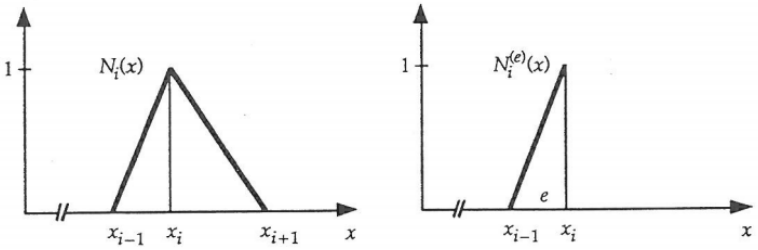

Figure 4.3: Global shape function on the left and local shape function of one element on the right [28].

In 1D the distance between nodes define the elements of the mesh so that can be define a shape function for each element as in figure 4.3. The global shape function is the summation of each local function on the element as $N_i(x) = \sum_i N_i^e$. In 2D the same procedure can be extended to two variable x, y. The mesh also extended to the point i, j. The global shape function becomes $N_i(x, y)$ equal to the summation of each local one:

$$N_i(x, y) = \sum_{e=1}^{node} N_i(x, y)$$

The same rules applies to the 2D case, where the shape function has value one in the node i, j and zero on the rest (i.e. on the support made of elements around the node i, j). Shape functions can overlap and so that theirs supports, as in figure 4.4.

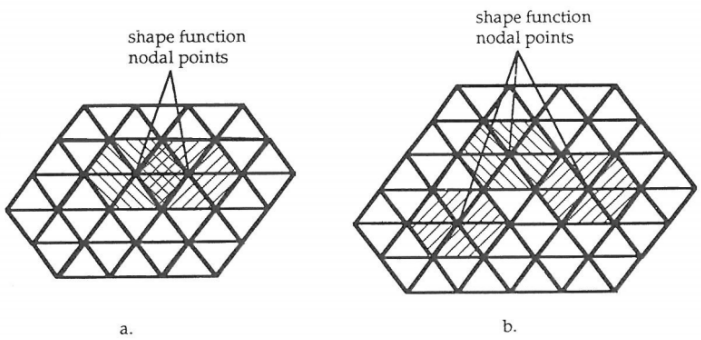

Figure 4.4: Supports with overlap on the left, without overlap on right [28].

The value of the global field $U(x, y)$ is the products between each shape function and the value of the field U_i on each node:

$$U(x,y) = \sum_{i=1}^{node} \left(\sum_{j=1}^{elements} N_i(x,y) \right) U_i \tag{4.8}$$

To reduce 4.7 to a linear system the *weight residual approach* is carried out. The operator $L(U) = \nabla \cdot \epsilon \nabla U + \delta = 0$ is defined in the electrostatic case for simplicity. With ϵ permittivity and δ source of charges. $L(U)$ is also zero if it's multiplied for the weight w such as:

$$\int_\Omega wL(U)\, d\Omega = 0 \tag{4.9}$$

Instead of the real potential U an approximated one is chosen like 4.8. Then the shape functions N can be assumed as weights w, chosen in a *finite number* equal to the node N. This is the called *Galerkin approach*. Eq.4.9 becomes:

$$\begin{aligned} &\int_\Omega N_i(\nabla \epsilon \nabla U + \delta)\, d\Omega = \\ &= \int_\Omega N_i \nabla \cdot \epsilon \nabla U \, d\Omega + \int_\Omega N_i \delta \, d\Omega \end{aligned} \tag{4.10}$$

Eq. 4.10 contains a double derivative as ∇^2. This can can introduce impulses if the function U is not continuous on the second derivative so that the "weak form" is introduced to lower the derivative order. Integrating by parts 4.10 becomes:

$$-\int_{\Omega} \epsilon \nabla N_i \nabla \cdot U \, d\Omega + \cancel{\int_{\Omega} N_i \delta \, d\Omega} + \cancel{\int_{\partial\Omega} N_i \epsilon \nabla U \mathbf{n} \, ds} \tag{4.11}$$

The last two terms cancel out, the first one because is a constant, the second one because it satisfies the Dirichlet condition in the boundaries $\partial\Omega$ ([28], § 4:2).
Finally introducing the approximated solution $U = \sum_j^N N_j U_j$ in 4.11, it becomes:

$$\int_{\Omega} \epsilon \nabla N_i (\nabla \sum_{j}^{N} N_j U_j) \, d\Omega = \sum_{j=1}^{N} \left(\int_{\Omega} \epsilon \nabla N_i \nabla N_j \right) U_j \, d\Omega = 0 \tag{4.12}$$

The quantity $\nabla N_i \nabla N_j$ is a derivation of shape function made of polynomials. This quantity, known as stiffness matrix $\mathbf{K}$, contains all the geometrical informations so that the whole system can be solved as an algebraic system

$$\mathbf{K} \cdot \mathbf{U} = \mathbf{b}$$

where the vector b contains boundary and source informations.

4.4 Magnetic force formulation

The first formulation of magnetic forces came up with the Lorentz force. With the spread of numerical methods Maxwell equations related to forces are almost validated even if the debate for the accuracy computation, especially with different material interfaces and non linear media, "is a more open subject"[31]. The first Lorentz formulation was correctly working in a model where the actual speed and current of each point was known. That's more a physical approach since the Lorentz force was initially build over a charge as Colombian force on particles. It means that the vectorial product between current and speed has to be known.
For the most variety of industrial application this approach isn't very useful since it is tricky to know these parameters for each point, furthermore if they are moving or laying in complex geometry. Relating the force computation to the magnetic field intensity allow to make this kind of computation suitable for the finite element method, since magnetic field and scalar potential are usually always known.

The formulation to derive forces from magnetics can be described by means of vectorial analysis. From Lorentz the force density per volume $[N/m^3]$ can be defined as:

$$f = \mathbf{J} \times \mathbf{B}$$

Introducing then the Ampere low solved for the current density J force becomes:

$$f = \frac{(\nabla \times \mathbf{B}) \times \mathbf{B}}{\mu_0}$$

Applying the constitutive equivalence of vectorial calculus it can be written as:

$$f = \frac{1}{\mu_0}\mathbf{B} \cdot \nabla\mathbf{B} - \frac{1}{2}\nabla\mathbf{B}^2 \tag{4.13}$$

By applying divergence theorem at 4.13 and switching to surface integral instead of volume one, the total force [N] become:

$$F = \int_v f \, dv \tag{4.14}$$

By integrating 4.13 and switching eq. 4.14 into a surface (S) integral the total force becomes:

$$F = \frac{1}{\mu_0}\int_s \left[B_n(B_n\mathbf{n} + B_t\mathbf{t}) - \frac{1}{2}(B_n^2 + B_t^2)\mathbf{n}\right] ds \tag{4.15}$$

$$= \int_s \frac{1}{\mu_0}B_n^2\mathbf{n} - \frac{1}{2\mu_0}B_n^2\mathbf{n} + \frac{1}{\mu_0}B_nB_t - \frac{1}{2\mu_0}B_t^2\mathbf{n}\, ds \tag{4.16}$$

$$= \int_s \frac{1}{2\mu_0}(B_n^2 - B_t^2)\mathbf{n} + \frac{1}{\mu_0}B_nB_t\, ds \tag{4.17}$$

With $\mathbf{B} = B_n\mathbf{n} + B_t\mathbf{t}$. The quantity of 4.17 out of integration is defined as Maxwell Stress Tensor τ. The stress tensor in a Cartesian frame becomes:

$$\tau = \frac{1}{\mu_0}\begin{bmatrix} B_x^2 - \frac{B^2}{2} & B_xB_y & B_xB_z \\ B_yB_x & B_y^2 - \frac{B^2}{2} & B_yB_z \\ B_zB_x & B_zB_y & B_z^2 - \frac{B^2}{2} \end{bmatrix} \tag{4.18}$$

It means that the stress tensor is a vectorial space with the information on the magnetic field components. The force acting on a volume immersed in a magnetic field is the divergence of the stress tensor within that volume, or its surface integral, if Gauss Theorem is applied:

$$F = \int_V \nabla\cdot\tau\, dv \xrightarrow{Gauss \quad T.} F = \int_{S=\partial V} \tau\mathbf{n}\, ds$$

Since electrical machine are in usually studied in two dimension, the tensor is dependent only on x and y and the integration become easier. Cylindrical volume, like the air-gap of a machine, can be integrated in a circumference inside the air-gap. With this assumption the main issue is the accuracy and the choice of the path of integration.

Then the tensor can be splitted (in two dimension) between radial and tangential component with L thickness of the surface:

$$F_n = \frac{L}{2\mu_0}\int_l B_n^2 - B_t^2\, dl \tag{4.19}$$

$$F_t = \frac{L}{\mu_0}\int_l B_tB_n\, dl \tag{4.20}$$

The tangential component of the stress tensor is useful to compute the torque on a electrical machine. By choosing a line of integration in the air-gap the torque become:

$$T = \frac{L}{\mu_0}\int_0^{2\pi} B_tB_n \cdot r^2\, d\theta$$

Because FEM solver solves the Maxwell equation for the potential A, the flux density B is computed numerically as derivation. Numerical derivation is not accurate so that variation up to 50% from the average torque value could be introduced [32].

To overcome this the "Arkkio mode" can be implemented, and it has already been done in some commercial FEM. It extends the integration over the air-gap surface instead that over a line:

$$T = \frac{L}{\mu_0(r_{out} - r_{in})} \int_0^{2\pi} \int_{r_{in}}^{r_{out}} B_n B_t \cdot r^2 \, dndt$$
$$= \int_S B_n B_t \cdot r^2 \, ds$$

With S air-gap surface.

Chapter 5

Stress review and formulation

5.1 Stress, Magnetics and Material

In this chapter the mechanical stress from the point of view of electrical machine is introduced. Stress is a condition in which a surface is submitted to a force $[\frac{N}{m^2}]$, therefore this quantity can introduce changes or breakdown in the material under analysis.
The usage of electrical machine to high speed rotation can introduce stresses to their mechanical parts such as rotor and stator.
The applied mechanical stress to magnetic materials introduce changes into the material itself, like magnetization curve, and therefore changes in the induction itself. When multiphysics and coupled phenomena occurs, one mathematical model is not enough anymore, so that this magnetic changes has been investigated with an amount of theory and results that goes beyond this work.
One of the main difficulty relies in the fact that mechanical stress can be caused by different sources. The external one such as mechanical unbalance of the machine, but also the magnetic field itself, that can actuate forces and thus mechanical deformation (magnetostriction).
The major material changes in hysteresis cycle can be described by fig5.3, where the magnetization were measured for different level of applied stress in iron.

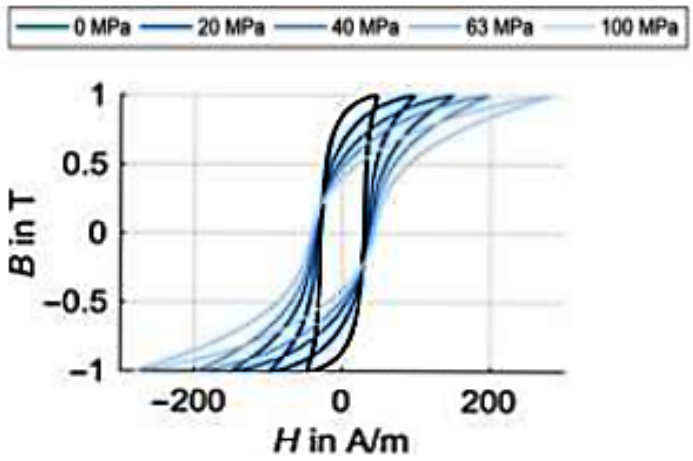

Figure 5.1: Hysteresis magnetization curve of M250-35A iron under differents applied stress at 50Hz [33].

The magnetic permeability has therefore the ability to increase under applied stress in a non linear way. But this improvements also tents to saturate, as the permeability itself. This behaviour, can also be dependent on the angle between forces and magnetic induction. As proved in [34], where has been described how permeability μ can drop or increase with respect to the stress angle.
In figure below the changing in per unit of μ can be seen as the induction orientation occurs inside the rotor.

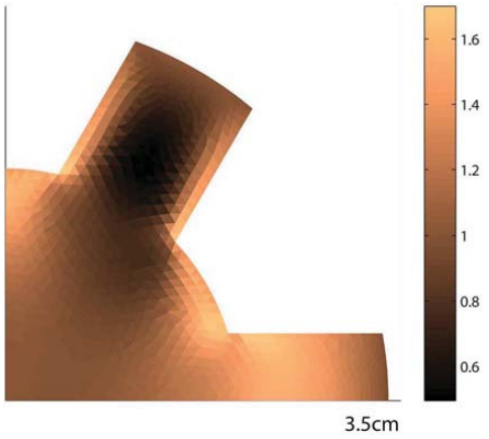

Figure 5.2: Relative permeability $\mu_{pu} = \frac{\mu_{stress}}{\mu}$ with a stress of 30 MPa, compressing towards the iron sheet at 30k rpm [34]. It's greater with uniaxial stress and lower with biaxial one.

With this assumption the constitutive magnetic law becomes stress dependent as:

$$B = \mu H \longrightarrow B = \mu(\sigma, B)H$$

where the stress $\sigma[N/m^2]$ inside the material is described by the parallel ($\sigma_{//}$) and orthogonal ($\sigma_{\perp}$) component given by:

$$\begin{bmatrix} \sigma_{//} \\ \sigma_{\perp} \end{bmatrix} = \mathbf{E} \cdot \begin{bmatrix} \epsilon_{//} \\ \epsilon_{\perp} \end{bmatrix},$$

$$\mathbf{E} = \frac{E}{1-\nu^2} \cdot \begin{bmatrix} 1 & \nu & 0 \\ \nu & 1 & 0 \\ 0 & 0 & \frac{1-\nu}{2} \end{bmatrix}$$

Here E is elasticity and ν the Poisson ratio.
In figure below the variation of scalar vector potential A has been simulated as difference between healthy and stress (due to centrifugal forces in this case) condition with 50Hz current load. It can be noticed an increasing right on the shaft close to the air barriers and more in general in proximity of the d-axe.

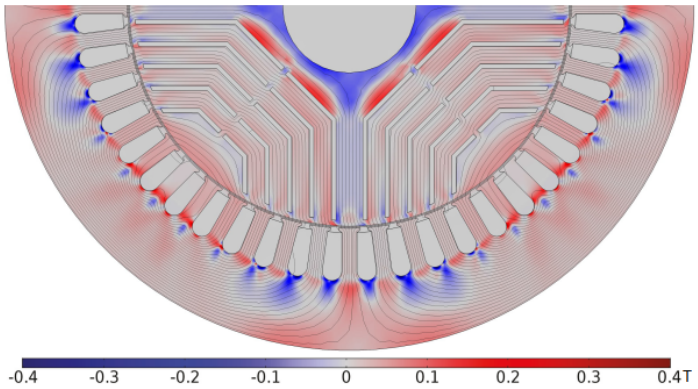

Figure 5.3: Induction error between healthy and faulty case in Tesla [35].

5.2 Stress Formulation

The stress here computed in this project is not related to the magnetic changing *inside* the materials, in their constitutive low. It's computed as stress acting on surfaces of the machine. As result of a mechanical misalignment of the rotor, and thus as result of forces acting *on* the machine.

Taking the Maxwell stress tensor surface integral, the total force in a surface S enclosing the air-gap is given by:

$$F = \int_S \left(\frac{B_n^2 - B_t^2}{2\mu_0} \cdot \mathbf{n} + \frac{1}{\mu_0} B_n B_t \cdot \mathbf{t} \right) ds$$

with **n** and **t** versor of the normal and tangential direction over the surface. Therefore from the tensor integration the radial and shear component of the stress can be derived respectively as

$$\sigma_n = \frac{1}{2\mu_0} \cdot (B_n^2 - B_t^2)$$
$$\sigma_t = \frac{1}{\mu_0} \cdot B_n B_t$$

The tangential one will be here neglected because is less relevant when it comes to forces. In this approach the spatial, but yet time dependent, stress distribution is carried out in a two-dimensional Fourier series as below:

$$\begin{aligned}\sigma_r = \sum_{m=0}^{\infty} \sum_{n=1}^{\infty} \lambda_{mn} [& a_{mn} cos(mp\phi) cos(n\omega t) + ... \\ & ... + b_{mn} cos(mp\phi) sin(n\omega t) + c_{mn} sin(mp\phi) cos(n\omega t) + ... \\ & ... + d_{mn} sin(mp\phi) sin(n\omega t)].\end{aligned}$$

The wave depending on m are the spatial terms, while the ones depending on n are those one related to time quantity, such as the synchronous speed of the magnetic field. All the coefficients are constants of integration given by:

$$\begin{cases} a_{mn} = \frac{p\omega}{2\pi^2\mu_0 r^2} \int_0^{\frac{2\pi}{p}} \int_0^{\frac{2\pi}{\omega}} \sigma_r cos(mp\phi) cos(n\omega t)\, d\phi dt \\ b_{mn} = \frac{p\omega}{2\pi^2\mu_0 r^2} \int_0^{\frac{2\pi}{p}} \int_0^{\frac{2\pi}{\omega}} \sigma_r cos(mp\phi) sin(n\omega t)\, d\phi dt \\ c_{mn} = \frac{p\omega}{2\pi^2\mu_0 r^2} \int_0^{\frac{2\pi}{p}} \int_0^{\frac{2\pi}{\omega}} \sigma_r sin(mp\phi) cos(n\omega t)\, d\phi dt \\ c_{mn} = \frac{p\omega}{2\pi^2\mu_0 r^2} \int_0^{\frac{2\pi}{p}} \int_0^{\frac{2\pi}{\omega}} \sigma_r sin(mp\phi) sin(n\omega t)\, d\phi dt \end{cases}$$

All the constants are time t, rotating field speed ω, pole-pairs p, and λ given by the cases below:

$$\lambda_{mn} = \begin{cases} \frac{1}{4} & for \quad m = n = 0 \\ \frac{1}{2} & for \quad m = 0, n > 0 \quad and \quad m > 0, n = 0 \\ 1 & for \quad m, n > 0 \end{cases}$$

The constant m and n appear in the sinusoidal or co-sinusoidal argument, so that they are responsible for the periodicity of the spacial displacement over the stator, or the time rotation of this displacement. λ is dependent both from the stress profile and its rotation. Managing this coefficient the Fourier series become [36]:

$$\sigma_r = \sum_{m=0}^{\infty}\sum_{n=1}^{\infty}\{\frac{\lambda_{mn}}{2}[(a_{mn}+d_{mn})^2+(b_m n - c_m n)^2]^{1/2}\cdot cos(-mp\phi + n\omega t + \ni_+) + \\ + \frac{\lambda_{mn}}{2}[(a_{mn}+d_{mn})^2+(b_m n - c_m n)^2]^{1/2}\cdot cos(-mp\phi + n\omega t + \ni_-)\}.$$

The different modes of the Fourier series will be described theoretically while the frequency components will be simulated.
In the mode zero ($m = 0$) the stress σ is constant, as figured in the scheme below:

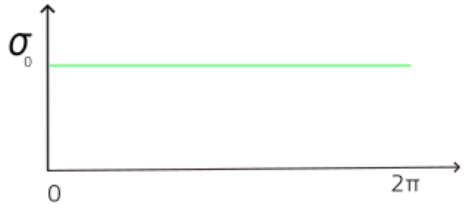

Figure 5.4: Stress profile σ_0 the over stator angular position.

This lead to a constant shrinking of the stator applied all over its surface as figured in 5.5

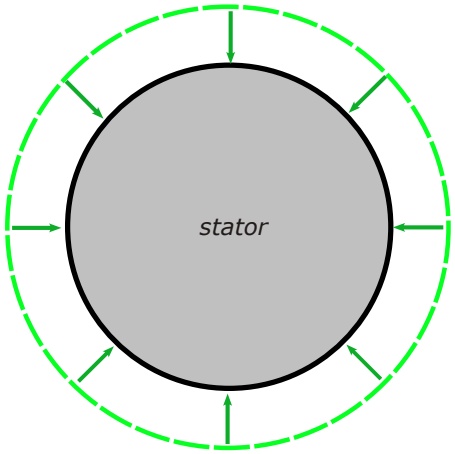

Figure 5.5: The positive constant stress (green dashed line) tents to compress the stator.

For $m = 1$ the stress profile has one period distribution over the stator. Respectively as figures below.

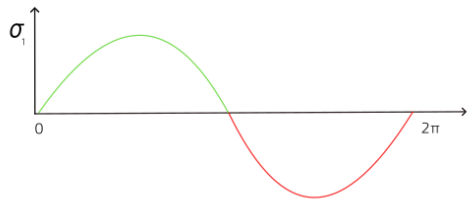

Figure 5.6: Stress profile σ_1 over the stator angular position. Here the average (positive) value is neglected.

This lead to pulling half of the stator from one side as figured below: the dashed line represents the average value of the stress acting on the stator. The green line represents the stress profile of the mode 1, for 180° greater than the average value and for the rest lower.

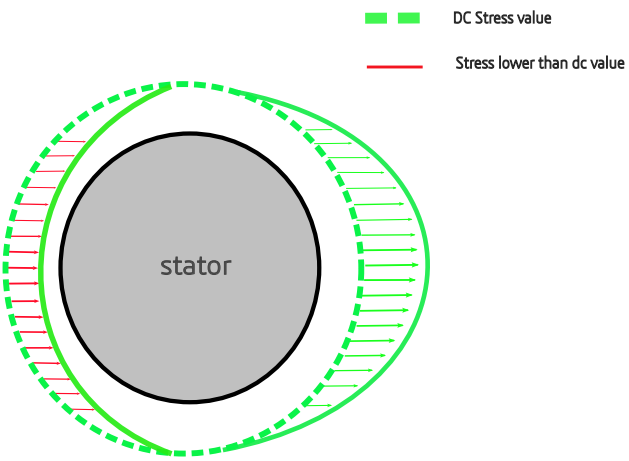

Figure 5.7: Stress profile σ_1 over the stator angular position.

The last mode simulated for $m = 2$ has two period over the stator angle:

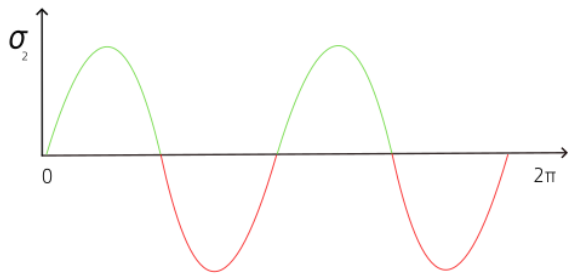

Figure 5.8: Stress profile σ_2 over the stator angular position.

This translates into the squeezing of the stator and pulling it within a rotation of 180° degrees. The same criteria of fig. 5.8 is assumed where the dashed line represents the average value.

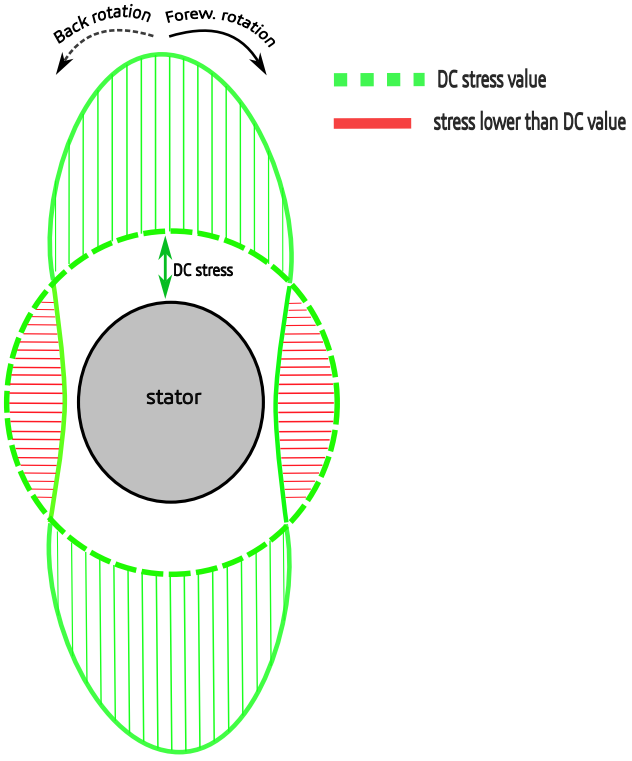

Figure 5.9: σ_1 profile over the stator angular position. The positive stress tents to pull the stator, the negative one tents to squeeze it.

In mode 2 also the backward rotation has been figured and simulated. All the stress profile is rotating along the profile. Roughly speaking this phenomena can be seen as a mono-phase quantity. When a quantity is alternating can also be described, mathematically, as a decomposition of two phasor of the same length rotating in opposite direction.

Chapter 6

Simulation and Results

6.1 Machine Parameters and Geometry

The machine analyzed is a synchronous reluctance motor with four pole and four barriers per pole. The main parameters are stated in table below:

Motor	Data
D^{ext}_{stator}	219 mm
D^{in}_{stator}	136 mm
D^{ext}_{rotor}	135.2 mm
D^{in}_{stator}	45 mm
Stator Slots	36
Pole	4
Air-gap	0.4 mm
Apparent Power	14.7 kVA
Active Power	10.6 kVA
Reactive Power	10.2 kVA
$cos\phi$	0.718
Rated Voltage	400 V (rms)
Speed	1500 rpm
Load angle	138°

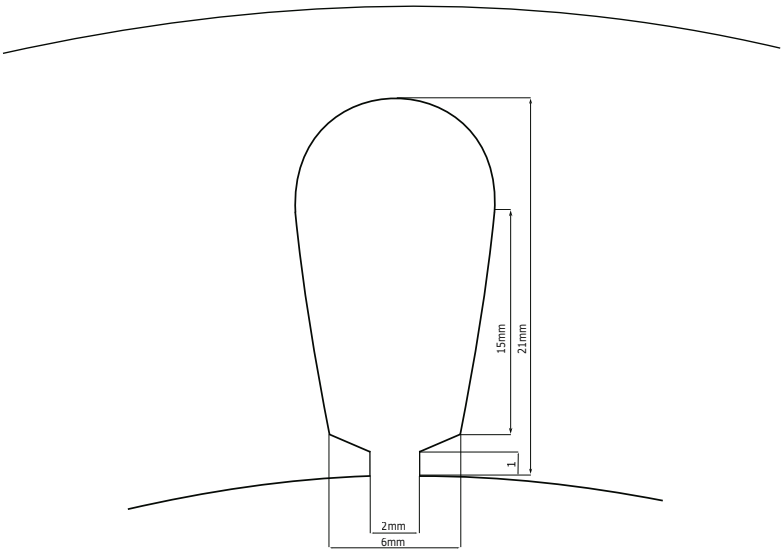

Figure 6.1: Slot measure.

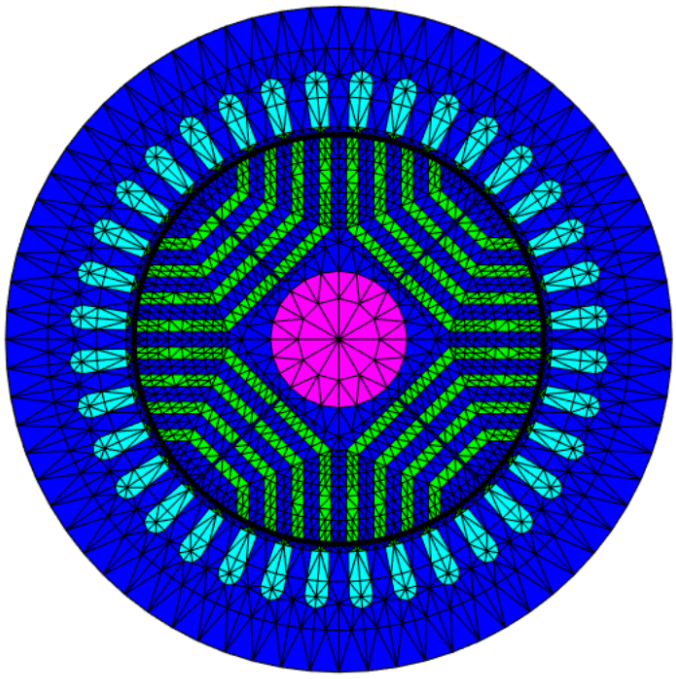

Figure 6.2: Machine mesh.

6.2 Simulation

To do the simulations an in-house solver (FCSmek) developed by professor Antero Arkkio has been used. It has the possibility to solve PDEs both in stationary and also time dependent domain. It has been developed in Fortran and linked to Matlab and VisualStudio for compiling and post-processing. The main workflow is the following:

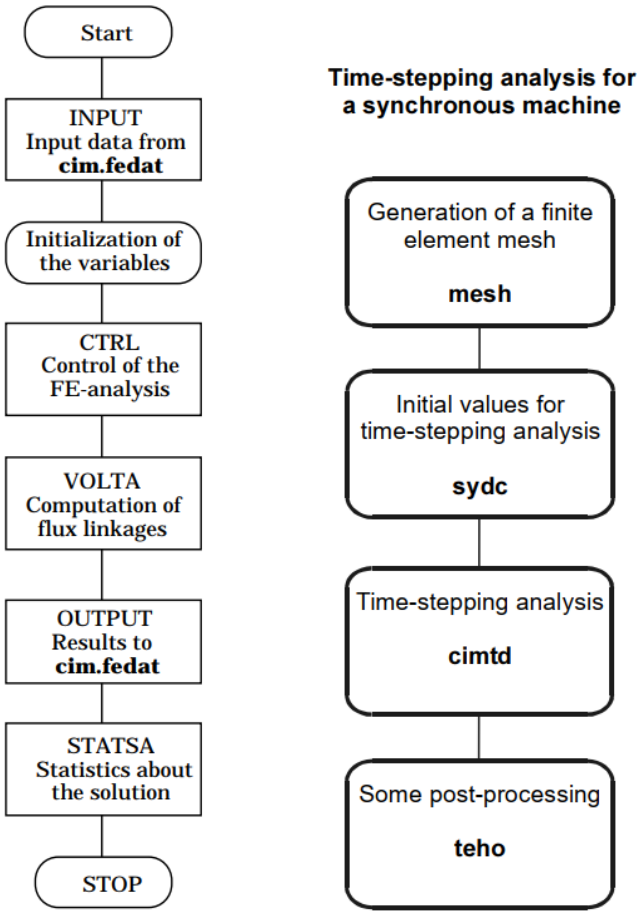

(a) (b)

Figure 6.3: a) Main workflow of the solver form the reference manual. The program is builded up in differents folders that contain informations both on input and output processed by the compiler. b) Workflow for the time-step analysis.

First has been computed the stationary analysis by the routines sydc, then the time dependent one by the cimtd routine. Both with the same input value, a mesh with second order elements, and temperature of both rotor and stator at 100° C.

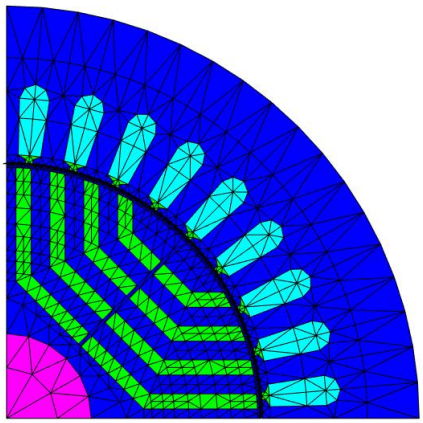

(a) *Machine mesh*

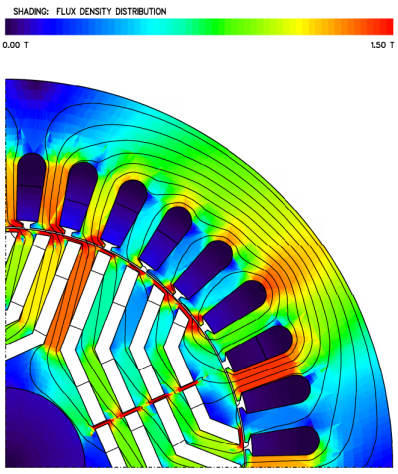

(b) *Induction map [T]*

Figure 6.4

The main parameters of the machine has been simulated in healthy case, like linkage voltage, synchronous speed and torque. The machine has been supplied by 400V (RMS) in star connection:

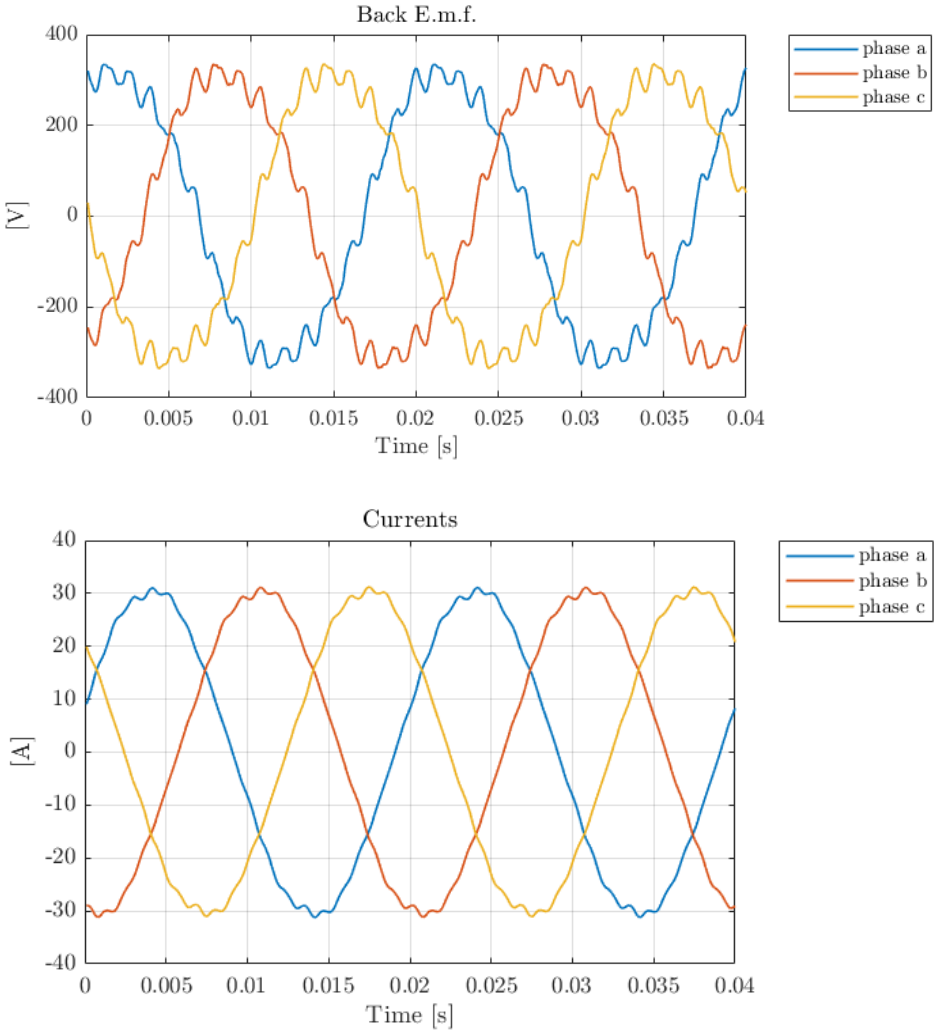

Figure 6.5: Three phase quantities of the machine at rated conditions.

The torque shows a ripple around 30-40%. By switching the eccentricity order δ in 3.1 to 50%, the ripple has an increasing of almost 3%. The average value of torque doesn't change and thus the performance overall. Torque ripple is computed as:

$$T^{\%}_{ripple} = \frac{T_{max} - T_{min}}{T_{average}} \cdot 100$$

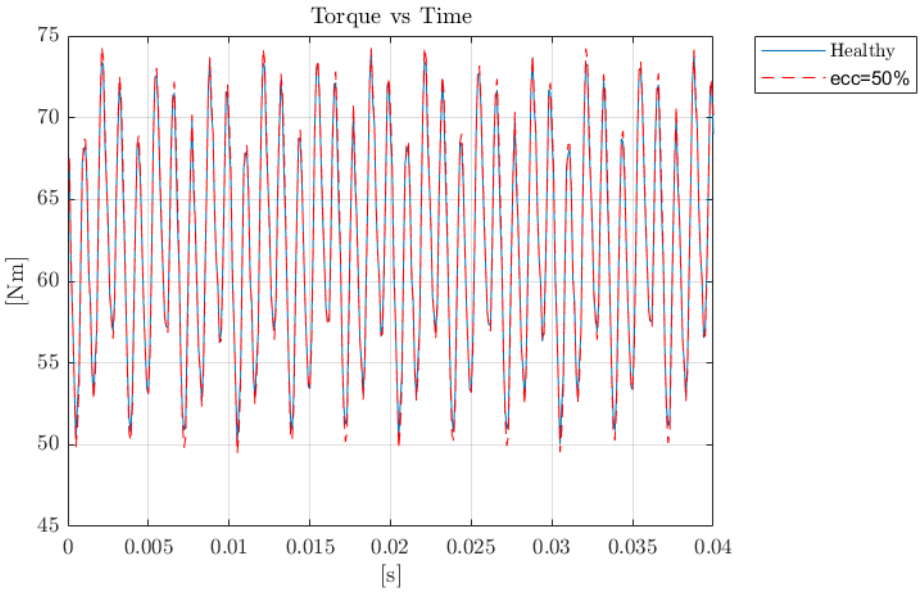

Figure 6.6: Torque ripple in healthy case and for eccentricity $\delta = 50\%$.

Subtle changes can be observed in the current amplitude, almost in the fundamental harmonic. It could be due to the fact that the concatenated flux doesn't change too much from the point of view of the stator winding.

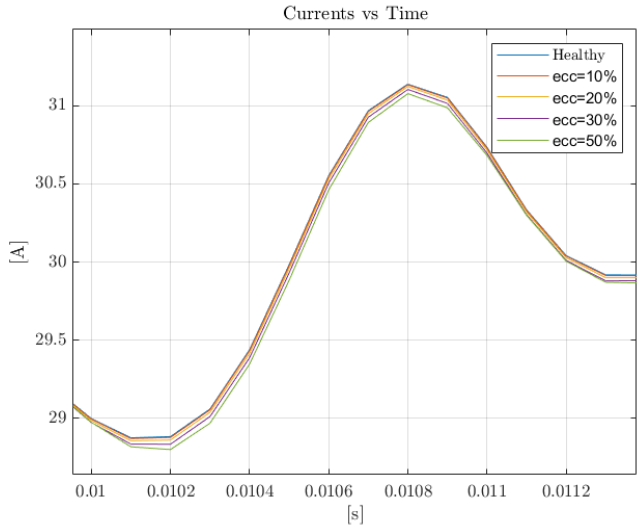

(a)

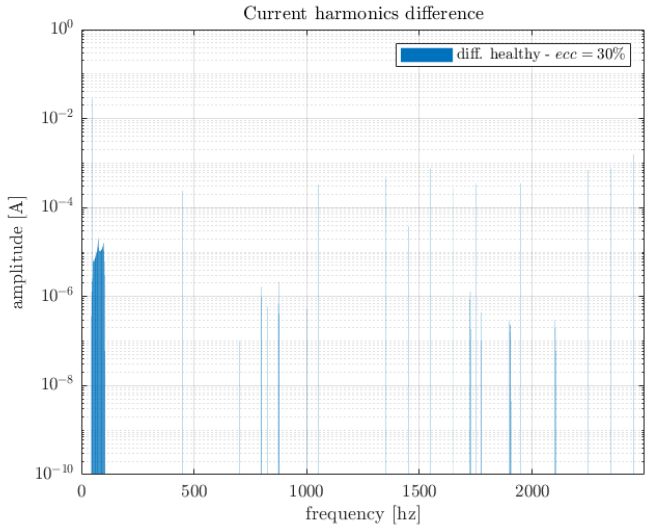

(b)

Figure 6.7: a) Up-close of the current for different eccentricity orders. b) Difference in current harmonics by means of fast Fourier transform between healthy and eccentricity case at 30%.

Forces has been computed trough the Maxwell stress tensor. Since the eccentricity is radial along the x-axe, the tangential force F_y is almost zero beside noises. On the other hand F_x has a significative increasing with the increasing of δ as expected:

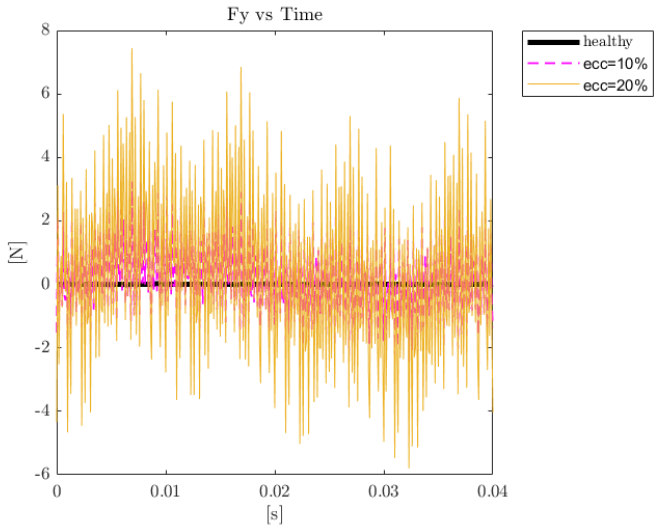

(a)

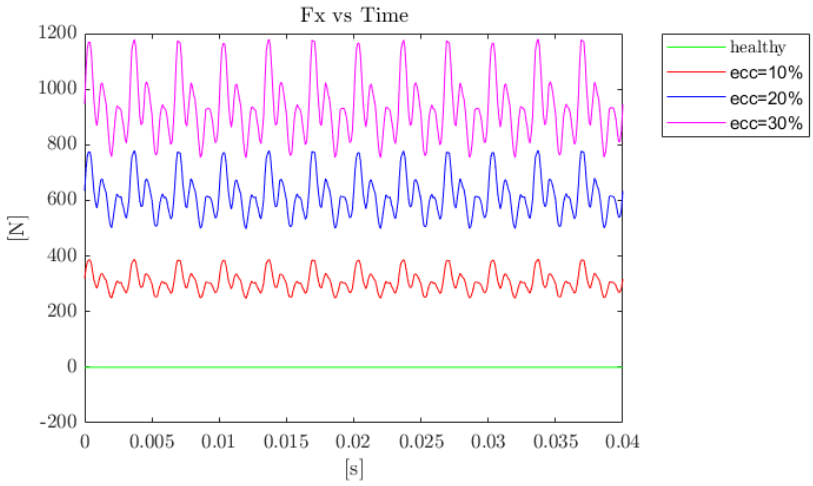

(b)

Figure 6.8: a) F_y tangential distribution is null for healthy case, it increases in terms of noise for eccentric case but with average value zero. b) F_x shows a significant increasing for different orders of eccentricity.

The fast Fourier transform (FFT) has been applied to F_x to see the most relevant harmonics:

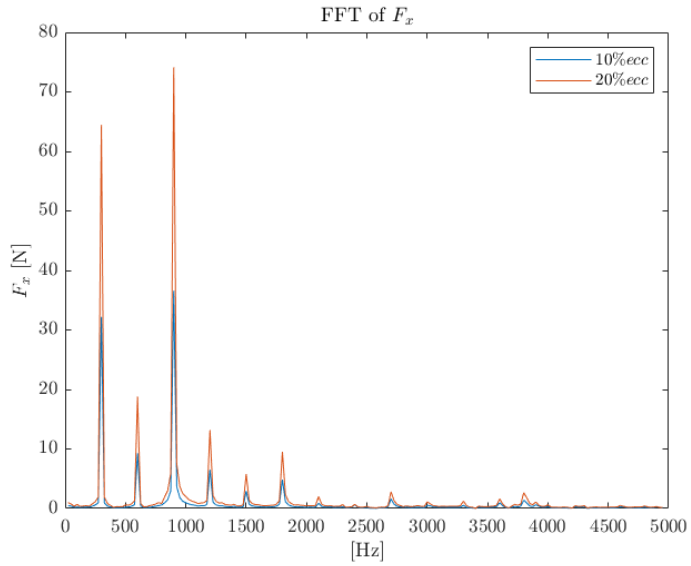

Figure 6.9: Frequency harmonics of F_x. A relevant spike around 300Hz and 900Hz can be noticed.

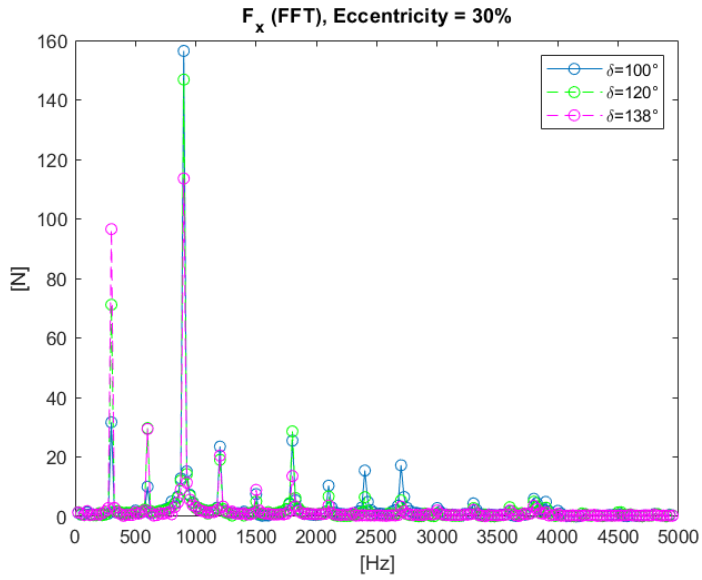

Figure 6.10: FFT of F_x with different load condition by changing the load angle. Nominal power of the machine reached for load angle at 138°.

As far as the stress is concerned, the stress mode discussed in chapter 5 has been simulated in a frequency domain. Below mode 0, mode 1 and mode 2:

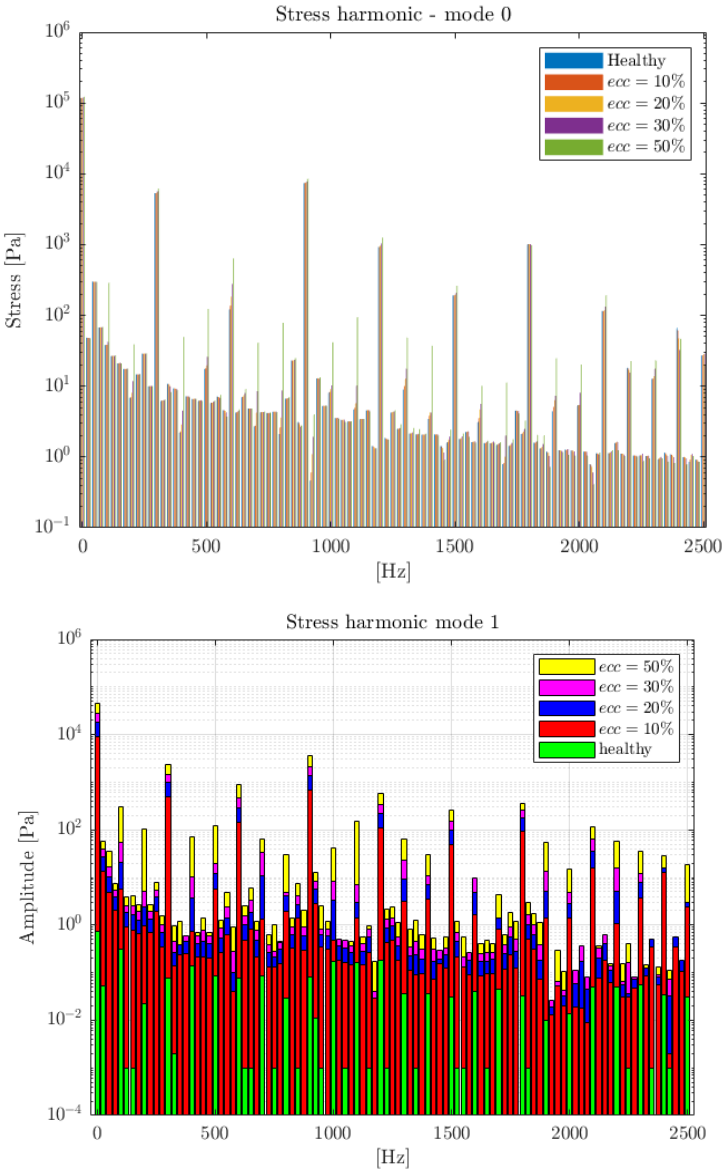

Figure 6.11: Mode 0 and mode 1 stress distribution. In mode 0 the main difference between healthy and eccentric case appears around 600 Hz, especially for ecc. = 50%. In mode 1 the difference between healthy and eccentric condition are more evident for each harmonic and most in particular for 900Hz.

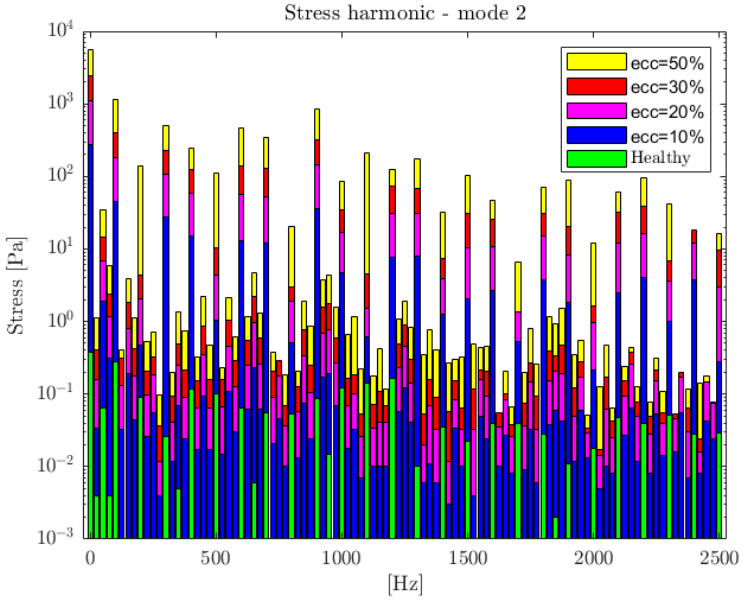

(a)

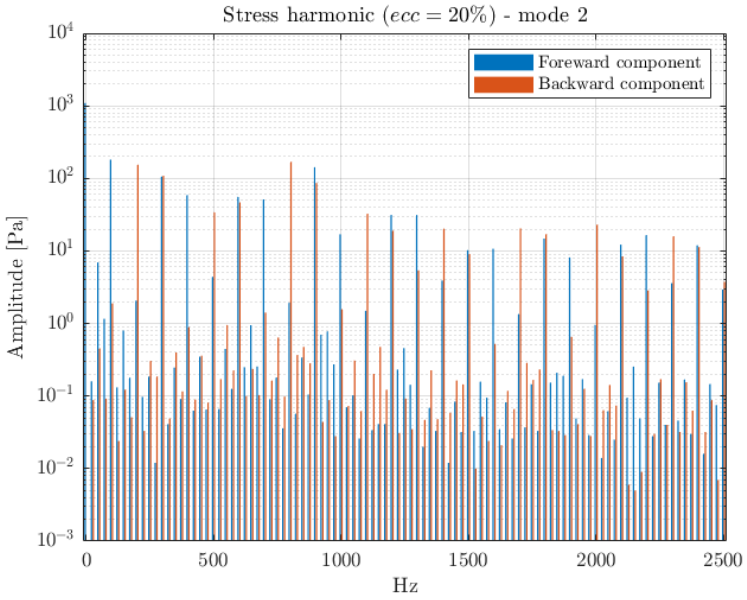

(b)

Figure 6.12: a) Same Fourier distribution for mode 2 with different order of eccentricity b) Stress distribution in mode 2 with eccentricity at 20% but with also the backward rotation simulated.

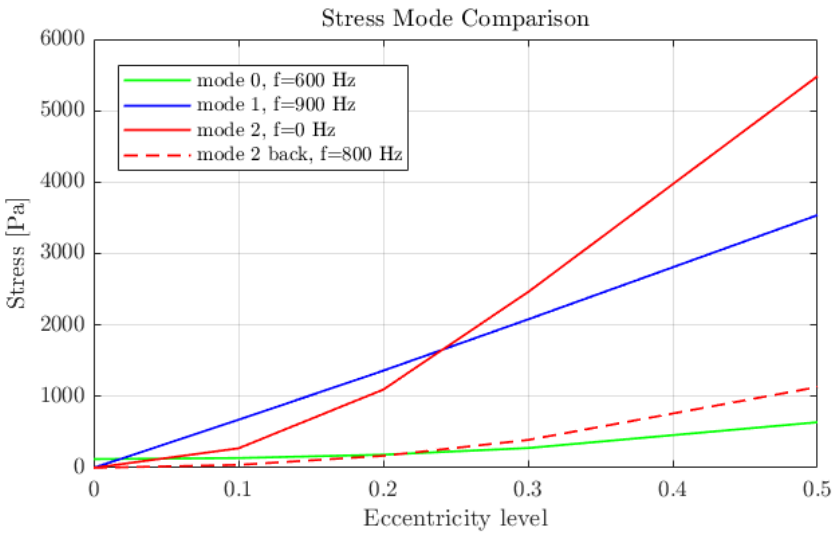

Figure 6.13: Comparison between the different stress modes with respect both to frequency and the eccentricity level up to 50%.

Chapter 7

Conclusion and future work

In this thesis project a synchronous reluctance machine has been investigated for different level of the eccentricity order. First the electromchanical force for each case, healthy and eccentric, were computed and then the relative stresses. A clear match has been shown between the frequency domain of forces and that one of stresses. Most in particular around 300Hz, 600Hz and 900Hz. A mode analysis has been carried out for the different periodicity of the stress distribution along the stator surface, in order to identify which one was the most relevant. The mode 0 seems the most relevant since it grows exponentially, but only on the fundamental. If we go further in frequency instead, the mode 1 seems the relevant one. The mode 2 is less effective at high frequency. The mode zero where the stator shrinking is constant doesn't seems to be affected by relevant changing between healthy and faulty case. The other two modes (m=1, m=2) have a more reactive response with the increasing of eccentricity. This could be due to the fact that for m=1 and m=2 the radial stress follow the magnetic pole distribution at different periodicity. The load angle doesn't seems to affect the frequency of the force distribution as it does for the amplitude of the harmonics. By lowering the load angle and thus the rated active power, the lower harmonics in the radial force tend to increase slightly. Future work in this field are possible such as investigating the mechanical side, vibration and its relationship with the stress. Measurements on the machine could also take part as experimental validation. An analytical explanation for the appearing of some peculiar harmonics in the forces distribution is not given. A possibly explanation, nonetheless a possible field of investigation, can come from the design side of the machine, such as the interaction between the number of slots and the air barriers. Given the fact that the more relevants harmonics are located below one kHz, their nature could also lay in the natural frequency of resonance of the whole rotating system, and so mostly in its mass.

Bibliography

[1] Hanafy Mahmoud and Nicola Bianchi. Eccentricity in synchronous reluctance motors—part I: Analytical and finite-element models. *IEEE Transaction on Energy Conversion*, Vol. 30, NO. 2, june 2015.

[2] Nicola Bianchi, Silverio Bolognani, Enrico Carraro, Mose Castiello and Emanuele Fornasiero. Electric vehicle traction based on synchronous reluctance motors. *IEEE Transactions on Industry Applications*, Vol. 52, NO. 6, november/december 2016.

[3] Bashir Mahdi Ebrahimi, Jawad Faiz and Mehrsan Javan Roshtkhari. Static dynamic and mixed-eccentricity fault diagnoses in permanent-magnet synchronous motors. *IEEE Transactions on Industrial Electronics*, Vol. 56, NO. 11, november 2009.

[4] Bashir Mahdi Ebrahimi, Jawad Faiz and Mehrsan Javan Roshtkhari. Vibration analysis of permanent-magnet-assisted synchronous reluctance machines. *IEEE 2019 22nd International Conference on Electrical Machines and Systems (ICEMS).*

[5] Tae-Jong Kim, Sang-Moon Hwang, Kyung-Tae Kim, Weui-Bong Jung, and Chul-U Kim. Scomparison of dynamic responses for ipm and spm motors by considering mechanical and magnetic coupling. *IEEE Transactions on Magnetics*, Vol. 37, NO. 4, july 2001.

[6] K Koskto. Polyphase reaction synchronous motors. *AIEE*, (Wagner Electric Corp & Co), 1923.

[7] Alfredo Vagati. Syncronous reluctance electrical motor having a low torque-ripple design. Patent 5,818,140, 6 ottobre 1998.

[8] S. Tahi , R. Ibtiouem. Finite element calculation of the dq-axes inductances and torque of synchronous reluctance motor. *IEEE*, (2014 International Conference on Electrical Sciences and Technologies in Maghreb (CISTEM), Tunis, Tunisia, 2014, pp. 1-5).

[9] Tae-Hee Lee , Jin-Hwan Lee , Kyung-Pyo Yi and Dong-Kuk Lim. Optimal design of a synchronous reluctance motor using a genetic topology algorithm. *Processes, 2021 9(10), 1778*, https://doi.org/10.3390/pr9101778.

[10] A. Boglietti, A. Cavagnino , M. Pastorelli , A. Vagati. Experimental comparison of induction and synchronous reluctance motors performance. *IEEE, Fourtieth IAS Annual Meeting. Conference Record of the 2005 Industry Applications Conference, 2005., Hong Kong, China, 2005, pp. 474-479 Vol. 1.*

[11] Thanh Anh Huynh and Min-Fu Hsieh. Comparative study of pm-assisted synrm and ipmsm on constant power speed range for ev applications. *IEEE 2017 Transactions on Magnetics*, vol. 53, no. 11, pp. 1-6, Nov. 2017.

[12] Shun Cai, Meng-Jia Jin, He Hao and Jian-Xin Shen. Comparative study on synchronous reluctance and pm machines. *COMPEL*, 35(2):pp. 607–623, 2016.

[13] Nicola Bianchi. Synchronous reluctance and interior permanent magnet motors. *IEEE Workshop on Electrical Machines Design, Control and Diagnosis*, 2013.

[14] Hanafy Mahmoud. Synchronous reluctance machines:eccentricity analysis and design criteria. *Doctoral Thesis, Università degli Studi di Padova*, 2017.

[15] Cristian Babetto, Giacomo Bacco, Nicola Bianchi. Analytical power limits curves of high-speed synchronous reluctance machines. *IEEE Transactions on Industry Applications*, vol. 55, no. 2, pp. 1342-1350, March-April 2019.

[16] H. Mahmoud and N. Bianchi. Nonlinear analytical model of eccentric synchronous reluctance machines considering the iron saturation and slotting effect. *IEEE Transactions on Industry Applications*, vol. 53, no. 3, pp. 2007-2015, May-June 2017, doi: 10.1109/TIA.2017.2666085.

[17] I. Coenen, M. van der Giet and K. Hameyer. Nonlinear analytical model of eccentric synchronous reluctance machines considering the iron saturation and slotting effect. *IEEE Transactions on Magnetics*, vol. 48, no. 5, pp. 1932–1936, May 2012.

[18] E. Rosenberg. Magnetic pull in electric machines. *Transactions of the American Institute of Electrical Engineers*, vol. XXXVII, no. 2, pp. 1425-1469, July 1918.

[19] D G Dorrell, W T Thomson and S Roac. Combined effects od a static and dynamic eccentricity in airgap flux waves and the application of current monitoring to detect dynamic eccentricity in 3-phase induction motors. *IEEE Electrical Machine and Drives*, 1995.

[20] A. Arkkio, Antila M., K. Pokki, Andy Simon. Electromagnetic force on a whirling cage rotor. *IEE Proceedings - Electric Power Applications 147(5):353 - 360*, 147(5):353 - 360.

[21] Mohamed Moustafa , Mahmoud Sedky. Diagnosis of static, dynamic and mixed eccentricity in line start permanent magnet synchronous motor by using fem. *International Journal of Electrical, Computer, Energetic, Electronic and Communication Engineering*, ,Vol:8, No:1, 2014.

[22] E. Pazouki, M. Z. Islam, S. S. R. Bonthu and S. Choi. Eccentricity fault detection in multiphase permanent magnet assisted synchronous reluctance motor. *2015 IEEE International Electric Machines Drives Conference (IEMDC)*, Coeur d'Alene, ID, USA, 2015, pp. 240-246.

[23] Hanafy Mahmoud and Nicola Bianchi. Analytical comparison of synchronous reluctance and surface permanent magnet machines with rotor eccentricity. *2015 IEEE Energy Conversion Congress and Exposition*, 2015.

[24] Anssi Sinervo. Effects of slotting and unipolar flux on magnetic pull in a two-pole induction motor with an extra four pole stator winding. *Aalto University, Doctoral Dissertation 77/2013*, 2015.

[25] Jaafar Hallal, Azri Hizami Rasid, Frederic Druesne, Vincent Lanfranchi. Comparison of radial and tangential forces effect on the radial vibrations of synchronous machines. *IEEE International Conference on Industrial Technology (ICIT)*, Melbourne, VIC, Australia, 2019, pp. 243-248.

[26] Jan-Ming Jin. *The finite elemnt method in electromagnetics*. Wiley, April 2014.

[27] Nicola Bianchi. *Electrical Machine Analysis Using Finite Element Method*. Taylor Francys Group, 2005.

[28] Jorma Luomi. *Finite Element Metod for Electrical Machine*. Göteborg 1993.

[29] Piergiorgio Alotto. *Computational Electrical Engineering-Lecture notes*. Università di Padova, 2021.

[30] Mustafa Kuzuoglu Ozlem Ozgun. *MATLAB-based finite element programming in electromagnetic modeling*. Taylor Francys Group, 2019.

[31] A. Bermúdez1, A. L. Rodríguez1, I. Villar. Extended formulas to compute resultant and contact electromagnetic force and torque from maxwell stress tensors. *IEEE Transactions on Magnetics*, Vol. 53, No. 4, 2017.

[32] Antero Arkkio. *Analysis of Induction Motors Based on the Numerical Solution of the Magnetic Field and Circuit Equations*, Doctoral Thesis, Helsinki, 1987.

[33] Jan Karthaus, Simon Steentjes, Nora Leuning and Kay Hameyer. Effect of mechanical stress on different iron loss components up to high frequencies and magnetic flux densities. *COMPEL*, Vol. 36, No. 3, pp. 580, 2017.

[34] Laurent Bernard, Xavier Mininger, Laurent Daniel, Guillaume Krebs, Frédéric Bouillault and Mohamed Gabsi. Effect of stress on switched reluctance motors: A magneto-elastic finite-element approach based on multiscale constitutive laws. *IEEE Transactions on Magnetics*, Vol. 47, No. 9, 2011.

[35] Deepak Singn. *Effect of Stress on Magnetic Properties of Electrical Steel Sheet and Core Losses in Electrical Machines*, Aalto University Doctoral Dissertation 280/2016.

[36] Anouar Belahcen. *Magnetoelasticity, Magnetic Forcers and Magnetostriction in Electrical Machines*, Doctoral Thesis, Helsinki University of Technology Department of Electrical and Communications Engineering Laboratory of Electromechanics, Report 72.